# Disentangling magnetic and environmental signatures of sedimentary 10Be/9Be records

Tatiana Savranskaia, Ramon Egli, Jean-Pierre Valet, Franck Bassinot, Laure Meynadier, Didier Bourlès, Quentin Simon, Nicolas Thouveny

Quaternary Science Reviews 257 (2021) 106809

Contents lists available at ScienceDirect

Quaternary Science Reviews

journal homepage: www.elsevier.com/locate/quascirev

# Disentangling magnetic and environmental signatures of sedimentary $^{10}Be/^{9}Be$ records

Tatiana Savranskaia [a, *], Ramon Egli [a, b], Jean-Pierre Valet [a], Franck Bassinot [c], Laure Meynadier [a], Didier L. Bourlès [d], Quentin Simon [d], Nicolas Thouveny [d]

[a] Institut de Physique Du Globe de Paris, CNRS, Université de Paris, 75005, Paris, France
[b] Central Institute for Meteorology and Geodynamics (ZAMG), 1190, Vienna, Austria
[c] Laboratoire des Sciences Du Climat et de L'Environnement (CEA-CNRS-UVSQ), Domaine Du CNRS, 91198, Gif-sur-Yvette, France
[d] CEREGE UM34, Aix Marseille Univ, CNRS, IRD, INRAE, Coll France, 13545, Aix en Provence, France

ARTICLE INFO

*Article history:*
Received 27 February 2020
Received in revised form
14 January 2021
Accepted 15 January 2021
Available online xxx

Handling Editor: A. Voelker

*Keywords:*
Cosmogenic nuclides
Beryllium
Authigenic $^{10}Be/^{9}Be$ ratio
Geomagnetic field intensity
Matuyama-brunhes reversal

ABSTRACT

Reconstructions of the global production rate of the cosmogenic isotope $^{10}Be$ from sedimentary records of authigenic $^{10}Be/^{9}Be$ ratios have been successfully used to obtain independent estimates of geomagnetic dipole moment variations caused by field excursions or reversals. In this study, we assess the reliability of $^{10}Be/^{9}Be$ as a proxy for the cosmogenic $^{10}Be$ production rate by evaluating two potential biasing sources represented by sediment composition and climatic modulation. For this purpose, we compare five high-resolution $^{10}Be/^{9}Be$ records of the Matuyama-Brunhes (M-B) field reversal from sediment cores of the Indian, West Pacific, and North Atlantic oceans. Significant increase of $^{10}Be/^{9}Be$ ratios at ~774 ka is explained in terms of the dominant control of geomagnetic modulation during the M-B reversal. Results do not support the existence of a direct proportionality between measured sedimentary $^{10}Be/^{9}Be$ ratio and cosmogenic $^{10}Be$ production rate, as shown by $^{10}Be/^{9}Be$ records that offset relative to each other during and outside the M-B reversal.

Residual differences between offset-corrected rescaled records do not appear to be related to an incomplete correction of variable sediment scavenging efficiencies by $^{9}Be$ normalization. Instead, these differences can be explained by a common climatic modulation model, assuming a linear relation between $^{10}Be/^{9}Be$ and the global $^{10}Be$ production rate with site- and time-dependent additive and multiplicative coefficients. These coefficients are linear functions of a single global climate proxy identified with the benthic $\delta^{18}O$ record. Additive coefficients are almost constant in time and can represent up to ~60% of the average $^{10}Be/^{9}Be$ value during periods of stable field polarity. Multiplicative coefficients are also site-specific, with mean values representing the bulk scavenging efficiency of the site, and variations about this mean expressing a multiplicative climatic modulation of the $^{10}Be$ production rate. The amplitude of this modulation amounts to 10–15% of the maximum variations recorded during the M-B reversal and is sufficiently large to mask minor variations of the dipole moment during stable polarity periods. Reconstructions of the geomagnetic dipole intensity can benefit from the information about climatic modulation effects gained with our modelling approach. Best suited sites for magnetic field reconstructions should be characterized by minimal Be-recycling contributions from ancient $^{10}Be$ reservoirs and minimal climatic modulation, as far as it can be determined from relative comparisons with other records. These conditions are most likely encountered in open basins at sites (1) with < 2.8 km water depth, (2) > 200 km offshore, and (3) located underneath a large current system extending over regions with minimum terrigenous inputs. Scaling all records with respect to a chosen reference enables to produce $^{10}Be/^{9}Be$ stacks with reduced noise and short-term local environmental effects. Differences between stacks obtained in this manner highlight global climatic effects that need to be considered when generating calibrated reconstructions of the geomagnetic dipole moment.



* Corresponding author.
*E-mail address:* savranskaia@ipgp.fr (T. Savranskaia).

https://doi.org/10.1016/j.quascirev.2021.106809

## 1. Introduction

Geomagnetic field intensity reconstructions over the last million years rely mostly on relative paleointensity (RPI) records that have been gathered for the past 30 years, and on their calibration with absolute paleointensity data, for instance from volcanic records (Valet, 2003). Production rate of cosmogenic nuclides offers an alternative way of tracking the geomagnetic intensity through time (Elsasser et al., 1956). The cosmogenic nuclide Beryllium-10 ($^{10}$Be) forms mostly in the atmosphere by a spallation process involving collisions of high-energy cosmic particles with nitrogen and oxygen atoms (Lal and Peters, 1967). The $^{10}$Be production rate depends on variations of the incoming flux of primary galactic cosmic rays, which is modulated by the geomagnetic field strength and by the solar activity (Kocharov et al., 1989; Beer et al., 2012; Lal and Peters, 1967; Blinov, 1988). During periods of low geomagnetic dipole strength and, therefore, lower cutoff-rigidity, the increased cosmic ray flux generates additional atomic collisions, increasing the cosmogenic nuclides production rate. The relationship between dipole strength and production rate is well constrained by cosmic ray trajectory calculations (Masarik and Beer, 1999, 2009; Poluianov et al., 2016). These calculations predict a $\sim$2.2$\times$ enhancement of the global $^{10}$Be production rate when the geomagnetic dipole moment decreases from its modern value ($\sim 7.8 \times 10^{22}$Am$^2$) to zero (Heikillä et al., 2009; Poluianov et al., 2016).

Once produced, cosmogenic $^{10}$Be is readily removed from the atmosphere by aerosols (Heikillä et al., 2008a) and, for the most part, by wet precipitation (Arnold et al., 1956; Goel et al., 1956; Heikillä and Smith, 2013). After reaching the Earth's surface, $^{10}$Be is further transported on land and in the oceans, where it is scavenged by suspended matter and finally deposited in sediments (von Blanckenburg and Bouchez 2014). Accordingly, the geomagnetic dipole moment can be reconstructed from properly normalized $^{10}$Be records using the geomagnetic modulation function obtained from production models (e.g. Raisbeck et al., 1985; Frank et al., 1997; Simon et al., 2020). A major advantage of this technique is that $^{10}$Be records are much less sensitive to local field anomalies than paleomagnetic reconstructions of the virtual axial dipole moment (VADM), owing to the global atmospheric redistribution of cosmogenic $^{10}$Be (Heikillä and Smith, 2013). On the other hand, the sedimentary $^{10}$Be flux is strongly modulated by atmospheric scavenging patterns (Field et al., 2006; Heikillä et al., 2009), by the transport paths on land and in the oceans (von Blanckenburg et al., 2012), and by the sediment scavenging efficiency (Anderson et al., 1990).

Scavenging of dissolved Be by suspended particles proceeds through incorporation in a continuously growing authigenic rim (Wittmann et al., 2017). The scavenging efficiency depends on particle size and composition (Mangini et al., 1984; Chase et al., 2002; Christl et al., 2003; Wittmann et al., 2012): opal and lithogenic phases are efficient beryllium scavengers contrary to $CaCO_3$ (Chase et al., 2002; Luo and Ku, 2004). The effect of scavenging efficiency variations can be eliminated by normalizing $^{10}$Be with the stable $^{9}$Be isotope that is released by weathering rocks (Measures and Edmond, 1983; von Blanckenburg et al., 2012) and uptaken by the same particles (Sharma et al., 1987). The isotopic ratio $^{10}$Be/$^{9}$Be obtained from the measurement of reactive Be selectively extracted from the authigenic rim is therefore identical to that of the dissolved isotopes (Southon et al., 1987; Bourlès et al., 1989a; Anderson et al., 1990; Ku et al., 1990; McHargue and Damon, 1991; Simon et al., 2016b, 2018a). Even so, the $^{10}$Be/$^{9}$Be ratio is not a globally homogeneous proxy of cosmogenic $^{10}$Be production, due to the different distribution of $^{10}$Be and $^{9}$Be sources, which make the two isotopes undergo different transport paths (von Blanckenburg and Igel, 1999; von Blanckenburg et al., 2012). These paths are responsible for systematic differences between ocean basins, and to a certain degree, within basins (Bourlès et al., 1989a; Ku et al., 1990; von Blanckenburg and Bouchez, 2014; von Blanckenburg et al., 2015; Simon et al., 2018b). As long as the beryllium redistribution patterns are constant over time, $^{10}$Be/$^{9}$Be records remain proportional to the global cosmogenic production rate and can be used for geomagnetic dipole moment reconstructions after proper site-specific normalization (e.g. Simon et al., 2016a; Simon et al., 2020). Climatic variations might change the beryllium redistribution patterns, introducing an unwanted environmental modulation that has never been properly quantified in marine sedimentary sequences.

The most direct evidence for the field recording capability of sedimentary $^{10}$Be/$^{9}$Be records comes from peak values corresponding to significant geomagnetic events, such as the last geomagnetic reversal (Matuyama-Brunhes, shortly M-B), recorded in marine sediments and loess deposits (Raisbeck et al., 1985; Carcaillet et al., 2004; Suganuma et al., 2010; Ménabréaz et al., 2014; Valet et al., 2014; Zhou et al., 2014; Simon et al., 2016a, 2018a) as well as in the EPICA Dome C polar ice core (Raisbeck et al., 2007). Here, we compare high-resolution sedimentary $^{10}$Be/$^{9}$Be records of the M-B reversal from the North Atlantic, Indian and Pacific oceans, showing that a site-specific normalization, on which current dipole moment reconstructions are based, is not sufficient for estimating the global $^{10}$Be production rate required by dipole moment reconstructions. We modeled pairwise differences between $^{10}$Be/$^{9}$Be records assuming that they contain two components: one that reflects differences in the efficiency with which freshly produced cosmogenic $^{10}$Be is transported to the ocean floor, and the other representing site-specific $^{10}$Be inputs that do not vary synchronously with the cosmogenic production rate. The first component is modulated by a single climatic proxy, identified with the oxygen isotope ratio, reflecting glacial-interglacial cycles. The second component must originate from $^{10}$Be reservoirs with residence times $>$100 ka or from the reactive transport of exchangeable Be within the sedimentary column. Once these components are identified, it is possible to isolate the synchronous response of individual records to variations of the global $^{10}$Be production rate and remove the differences between records caused by global climatic effects. The resulting corrected isotopic ratios can be stacked onto a suitably chosen reference record. While only relative differences caused by global climatic changes can be removed with this procedure, it is still possible to minimize the residual signal contamination. The gained information can be used to obtain optimised reconstructions of the geomagnetic dipole, as shown in a following article.

## 2. Environmental setting and lithology

The data set used in this study comprises five high-resolution beryllium records (Valet et al., 2014, 2019; Simon et al., 2018 a,b) and one record with lower sampling rate (Ménabréaz et al., 2014), obtained from piston cores from the Indian, western Equatorial Pacific and North Atlantic Oceans (Fig. 1) (Horng et al., 2002; Valet et al., 2014, 2016; Ménabréaz et al., 2014; Simon et al., 2018 a,b). Cores MD90-0949 (2°06.90′ N; 76°06.50′ E) and MD90-0961 (5°03.71′ N; 73°52.57' E) were collected during the SEYMAMA research cruise of the R/V Marion Dufresne in 1990. The 28-m long core MD90-0949 is dominated by green to gray calcareous nannofossil ooze with coccoliths and foraminifera while the non-carbonate fraction mostly consists of terrigenous clays and, to a lesser extent, biogenic silica (Bassinot, 1993). Core MD90-0961 is 45-m long and composed of calcareous nanofossil ooze with abundant foraminifera (Valet et al., 2014). It was retrieved on the eastern margin of the Chagos-Maldive-Laccadive Ridge, which

stretches nearly 3000 km (Backman et al., 1988) along the 73° meridian.

Core MD98-2183 (2°00.82′ N; 135°01.26′ E) was sampled by the R/V Marion-Dufresne in the West Caroline basin of the Western Pacific Ocean during the IMAGES IV cruise and consists of hemipelagic clay with calcareous and siliceous microfossils (Yamazaki and Oda, 2004). The basin is mainly influenced by nutrient supply from sinking particles in coastal regions in the Philippine and Indonesian Islands while the lithogenic input is dominated by clay minerals (Kawahata et al., 1998). The site is located on the path of the Equatorial counter current (surface/intermediate layer), which includes the west-east return current (Tchernia, 1980), the Atlantic Intermediate waters and the Upper Circumpolar Deep Water. The deep-water circulation is dominated by the Lower Circumpolar Water that partially proceeds along the southern boundary of the east Caroline Basin, flowing northward in the western East Caroline Basin (Kawabe et al., 2003). Core MD97-2143 was taken from the Benham Rise in the West Philippine Sea (15°52.26′ N; 124°38.96′ E) during the IMAGES III-IPHIS-Leg II Cruise. The site is characterized by the absence of significant bottom currents. The Benham Rise is 230 km away from Luzon Island, which has a narrow continental coast (Yu et al., 2016). The late Quaternary sediments are mainly composed of calcareous nannofossil ooze with foraminifera and volcanic debris (Wei and Lee, 1998). Terrigenous detrital material is virtually absent and minor amounts of pelagic clay confirm that the Benham Rise has been shielded from supply of terrigenous Luzon Island and other continental landmass detritus. Yu et al. (2016) carried out a clay mineralogy analysis of sediment from the closeby core MD06-3050 (15°57.09′ N, 124°46.77′ E) and concluded that the detrital material mainly originated from Luzon volcanic rocks and eolian dust from Asian deserts. Site MD05-2930 is located on the north coast of Papua New Guinea in the Bismarck Sea (2°51′ S; 144°32' E). This sedimentary sequence was retrieved at 1490 m water depth and is mainly consist of homogeneous gray-green clayey and silty clayey muds, rich in foraminifera (Ménabréaz et al., 2014).

Finally, core MD95-2016 is composed of a mixture of silt clay and nano-ooze. It was taken during the IMAGES I leg IV campaign in the North Atlantic Ocean (57°42.46′ N; 29°25.44' W) approximately 800 km away from the coast on the crest of the Reykjanes Ridge located on the pathway of the Iceland-Scotland Overflow water (Zou et al., 2017) which plays an important role for sediment composition and redistribution (Gehrke et al., 1996). At high northern latitudes, terrigenous input dominated during glacial periods in the northeast Atlantic Ocean. Turbidity currents, bottom currents, wind, and ice are potential transporters of terrigenous detritus from the continents (Ruddiman and McIntyre, 1976).

Additional beryllium-9 measurements from three cores were included in this study for comparison purposes. MD96-2077 (33°17′ S; 31°25′ E) was retrieved from 3781 m depth at the Natal Valley in the subtropical Indian Ocean during the MD105 (Images II) campaign. The sediments consist of nanno and nannofossil oozes with periodically occurring gray to brownish layers of mud and clay intraclasts, frequently bioturbated. Site ODP 851 (2°46′N; 110°34′ W) is located near the northern extent of the westward-flowing South Equatorial Current (SEC) and near the southern limit of the seasonal migration of the boundary between the North Equatorial Countercurrent (NECC). The sedimentary sequence can be described as a single lithologic unit composed of a mixture of foraminifer nannofossil and diatom nannofossil oozes (Mayer et al., 1992). Lastly, core MD05-2920 was retrieved in 2005 in the north coast of Papua New Guinea, in the Bismark Sea (2°51′ S; 144°32′ E). Sediments are mainly composed of homogenous greyish olive clay, with dispersed foraminifers and occasional black lenses of organic matter (Beaufort et al., 2005). The carbonate and terrigeneous fractions proportions are ~ 70% and ~ 25% respectively in the top core sediments (Tachikawa et al., 2011). The reader is referred to Ménabréaz et al. (2012, 2014) and Simon et al. (2016a, 2020) for Be data.

## 3. Methods and measurements

### 3.1. Beryllium isotope measurements

Samples of ~1 g dry sediment were processed for Be isotope analyses following the chemical procedure described in Simon et al. (2016b). The leaching technique of Bourlès et al. (1989a) allows extracting both isotopes in the phase that corresponds to the equilibrated authigenic fraction of soluble $^{10}$Be and $^{9}$Be. Approximately 70% and 40% of authigenic $^{10}$Be and $^{9}$Be, respectively, are carried by iron and manganese oxyhydroxides, and the rest is attributed to exchangeable and carbonated fractions (Bourlès et al., 1989b). Because both isotopes have identical chemical properties, $^{10}$Be/$^{9}$Be obtained by this technique is supposedly insensitive to downcore lithological changes (Henken-Meillies et al., 1990; Simon et al., 2016b). The natural authigenic $^{9}$Be concentration was measured using a graphite-furnace atomic absorption spectrophotometer (AAS) with double-beam correction. The $^{10}$Be

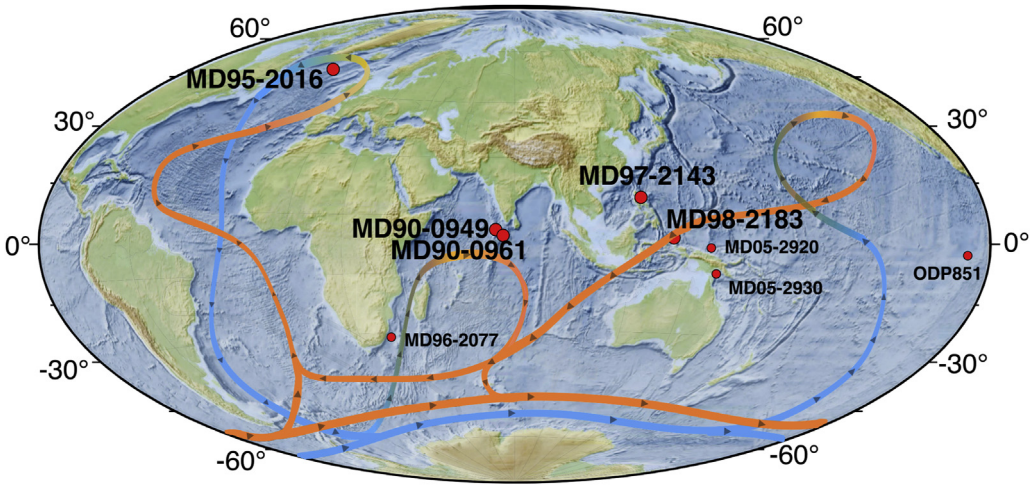


**Fig. 1.** Bathymetric map showing the location of investigated cores and the main oceanic currents. Sites marked with bigger font are the high-resolution records.

concentration was measured after chemical preparation at the French accelerator mass spectrometer (AMS) national facility ASTER (CEREGE). Chemistry blank ratios range from $10^{-14}$ to $10^{-15}$, what is at least 3 order of magnitude lower than the sample $^{10}Be/^{9}Be$ ratios. Concentration values were corrected for radioactive decay using the $^{10}Be$ half-life of 1.387±0.012 Myr (Chmeleff et al., 2010; Korschinek et al., 2010).

### 3.2. Oxygen isotopes and age model

Age-depth models for the five cores were established using high-resolution stable oxygen isotopic records from benthic and planktonic foraminifera species. Depending on the amount of available foraminifera, analyses were performed on a VG-Optima or an Elementar Isoprime dual-inlet mass spectrometer. All results are expressed as $\delta^{18}O$ with respect to the V-PDB standard. The external analytical reproducibility is ±0.05‰(1σ) as determined from replicate measurements of a laboratory carbonate standard. Astronomical age models for cores MD90-0949/961, MD95-2016 and MD98-2183 were derived by tuning the benthic $\delta^{18}O$ records of *Cibicides wuellestorfi* to the LR04 stack (Lisiecki and Raymo, 2005) using a two-steps approach (Simon et al., 2018b; Valet et al., 2019). First, uncalibrated depth-age models were constructed by assigning a common depth to all records after correlating the individual $\delta^{18}O$ records. The composite record of the sister cores MD90-0961/963 with the largest depositional rates and highest oxygen isotope resolution was then chosen as internal reference (Bassinot et al., 1994; Valet et al., 2014). Identification of the Australasian microtektite event (e.g. Valet et al., 2019) at the beginning of termination IX, the transition from the Marine Isotopic Stage (MIS) 20 to MIS19 provided an additional, independent tie-point for the two Indian Ocean cores. The limited thickness of the microtektite layer relative to the interval of increased $^{10}Be/^{9}Be$ values associated with the M-B reversal excludes significant smoothing effects over the transition timescale (Supplementary Fig. 1). In particular, the peak of $^{10}Be/^{9}Be$ records corresponding to the disappearance of the dipole field component is not expected to be affected by sediment mixing. After correlating all individual $\delta^{18}O$ profiles to the MD90-0961/0963 reference record, the age model was developed by tuning the benthic $\delta^{18}O$ record from MD90-0961/0963 depth scale to the LR04 stack. This strategy allowed us to represent all records on a common time scale using coherent stratigraphic approach. The age model for MD97-2143 was obtained after correlating its $^{10}Be/^{9}Be$ record with that of core MD90-0961. The average deposition rates derived from the age model of each core are summarised in Table 1. They are comprised between 1.2 cm/ka (core MD97-2143) and 3.8 cm/ka (core MD90-0961).

### 3.3. Calcium carbonate measurements

Calcium carbonate ($CaCO_3$) measurements were performed on samples taken at 4 cm intervals in cores MD90-0949, MD90-0961, MD95-2016, MD97-2143 and MD98-2183. The total carbonate content (in weight %) was determined from the pressure of $CO_2$ released through the reaction of 1 mg of dry grounded sediment with hydrochloric acid. $CaCO_3$ contents range from a few percents to more than 75% with small fluctuations in each core (Table 1). For comparison reasons, we added data from core MD05-2920 (western equatorial Pacific Ocean, 2.51°S, 144.32°E) (Tachikawa et al., 2011), ODP site 851D (eastern equatorial Pacific) (Mayer et al., 1992), and MD96-2077 (subtropical Indian Ocean, 33.17°S, 31.25°E) (Bard and Rickaby, 2009).

The scavenging efficiency of bulk sediment is affected by the carbonate content, owing to the much smaller partition coefficient of $CaCO_3$ ($K_d \approx 1–3 \times 10^4$ ml/g) with respect to other sedimentary components, such as lithogenic fractions (1.5–3.8 $\times$ $10^6$ml/g), organic matter ($\sim 22 \times 10^6$ ml/g) and biogenic silica (0.75–1 $\times$ $10^6$ ml/g) (Luo and Ku, 2004; Li et al., 2005). Indeed, we find a negative correlation between the $CaCO_3$ content and $^{9}Be$ concentrations in our sediments (Fig. 2a), similar to that expected from the binary mixture of low-$K_d$ $CaCO_3$ with other high-$K_d$ sedimentary components. The scavenging efficiency of sediments containing large amounts of biogenic carbonates is also affected by the $K_d$-independent incorporation of Be in foraminifera (Dong et al., 2001). Extrapolation of highly carbonated sediment data to 100% $CaCO_3$ yields a limit $^{9}Be$ concentration of up to 50 ppb ($3.3 \times 10^{15}$ at/g), compared to ~10 ppb ($0.67 \times 10^{15}$ at/g) measured in fresh foraminiferal calcite (Dong et al., 2001). As expected, $^{10}Be/^{9}Be$ is not systematically affected by the $CaCO_3$ content (Fig. 2b).

## 4. Sedimentary $^{10}Be/^{9}Be$ records of the M-B reversal

The underlying assumption of present $^{10}Be$-based geomagnetic dipole moment reconstructions is that $^{10}Be/^{9}Be$ is directly proportional to the global $^{10}Be$ production rate, due to the dominant dipolar control and fast atmospheric mixing. In this case, a site-specific, time-independent proportionality constant for each record can be empirically derived from the comparison of measured $^{10}Be/^{9}Be$ values with the $^{10}Be$ production rate predicted for a given time with known VADM, or with a long-term average. In this scenario, records of the same geomagnetic event, here the M-B reversal, should be proportional to each other. This is not the case, however, as seen from the maximum relative $^{10}Be/^{9}Be$ increase during the M-B transition with respect to background levels before (808–850 ka) and after (707–743 ka) this event (Fig. 3a), which ranges from ~150% for MD90-0949 to ~220% for MD90-0961. On the other hand, all records share very similar features during the M-B reversal (e.g. the main bell-shaped peak at ~774 ka and a shoulder at ~790 ka), and, for certain core subsets, also outside the reversal interval (e.g. at ~730 ka). These similarities suggest a common primary modulation of the $^{10}Be$ input. Differences between maximum relative increases of $^{10}Be/^{9}Be$ during the M-B reversal cannot be attributed to $^{9}Be$ normalization artifacts (Fig. 3b), nor do they correlate with oxygen isotope records (Fig. 3c). These observations might lead to the erroneous conclusion that $^{10}Be/^{9}Be$ records are not systematically affected by global climatic changes.

In the following, we describe a method for quantifying the different $^{10}Be/^{9}Be$ responses observed during the M-B reversal, and discuss possible relations with core location and sediment properties. We start with a linear rescaling procedure from which we

**Table 1**
Mean deposition rates ($v_{sed}$) deduced from the age model described in section 3.2, mean $CaCO_3$ content with variations measured within the indicated interval in the core, water depth ($H_w$), and distance to the nearest coast ($D$). The deposition rate for cores in italic and mean $CaCO_3$ value for MD96-2077 are taken from the references (Ménabréaz et al., 2012 (MD05-2920); Rickaby et al., 2007 (MD96-2077); Ménabréaz et al., 2014 (MD05-2930); Mayer et al., 1992 (ODP851)).

| core | $\mathbf{v_{sed}}$ | $\mathbf{CaCO_3}$ | core depth | $\mathbf{H_w}$ | D |
|---|---|---|---|---|---|
| | cm/ka | % | cm | m | km |
| MD98-2183 | 2±0.61 | 7.91±7.60 | 2980–3089 | 4388 | 328 |
| MD97-2143 | 1.2 ±0.26 | 21.52 ±11.2 | 1475–1634 | 2989 | 205 |
| MD90-0949 | 1.8±0.32 | 62.55±5.54 | 2022–2138 | 3600 | 280 |
| MD90-0961 | 3.8±0.49 | 63.93±2.68 | 3533–3800 | 2450 | 35 |
| MD95-2016 | 2.7±0.5 | 18±6.39 | 2997–3177 | 2318 | 760 |
| *MD96-2077* | 4.5±2.36 | 57±6.43 | 0–2780 | 3781 | 266 |
| *MD05-2920* | 13 | 34±6.12 | 1010–3610 | 1848 | 130 |
| *MD05-2930* | 4.4 | – | 3000–3500 | 1490 | 162 |
| *ODP851* | 1.8±0.41 | 78±7.47 | 1304–2100 | 3760 | 2200 |

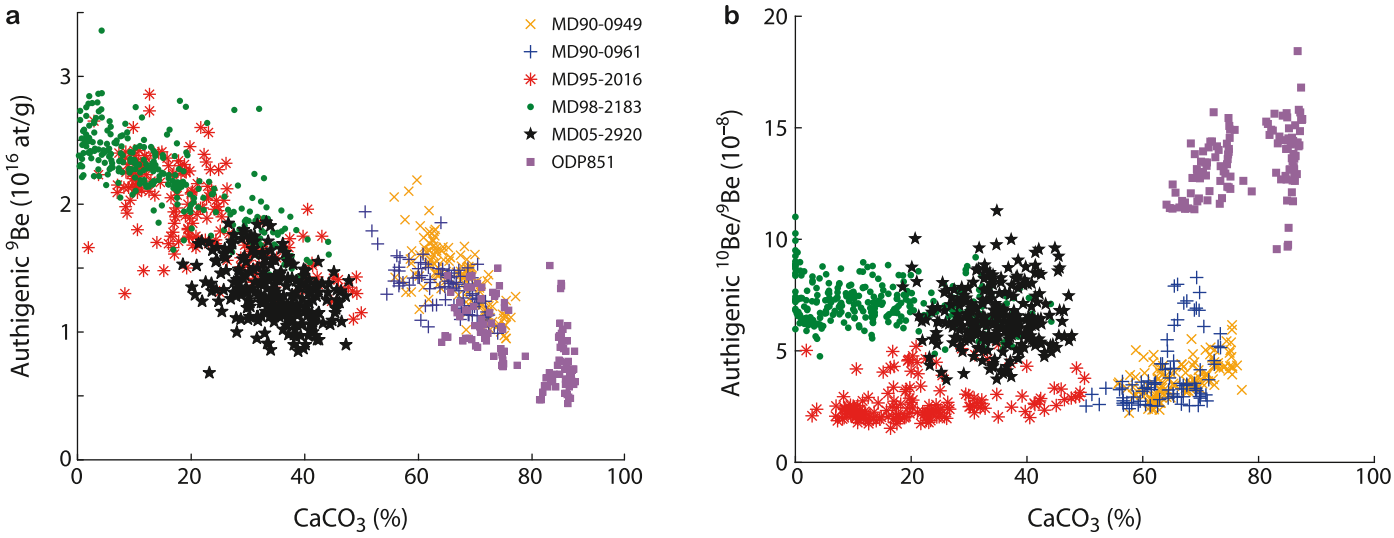


**Fig. 2.** Dependence of authigenic $^{9}$Be concentrations **(a)** and $^{10}$Be/$^{9}$Be (b) on the calcium carbonate content for individual specimens of six cores.

obtain site-specific, time-independent coefficients reflecting an additive and a multiplicative modulation of the original cosmogenic $^{10}$Be production rate. Next, we postulate that these coefficients are linear functions of a global climate proxy, taken to be $\delta^{18}$O, and show that all differences between sites can be explained by two mechanisms: a site-specific, nearly constant $^{10}$Be input that does not depend on the cosmogenic production rate, and a production-rate-proportional input that is mainly modulated by glacial-interglacial cycles. Finally, we discuss possible site-specific factors affecting these two inputs.

### 4.1. Linear scaling of $^{10}$Be/$^{9}$Be records

Obtaining a proper quantification of the $^{10}$Be/$^{9}$Be increase during the M-B reversal is not trivial, since maximum values are affected by short-term variations (particularly in MD98-2183), damped to various extents by site-specific, bioturbation-induced sediment mixing (Anderson, 2001; Christl, 2007). These problems are effectively overcome by considering the integral of the $^{10}$Be/$^{9}$Be excess during the M-B reversal. Because $^{10}$Be/$^{9}$Be is a lithology-insensitive proxy of $^{10}$Be concentration, it can be converted to a fluence, defined as the integral of sedimentary $^{10}$Be flux over time, where (flux) = (volume concentration)×(deposition rate). Mass conservation makes fluences insensitive to bioturbation-related smoothing effects (which are negligible in our records of the M-B reversal but not in the case of shorter geomagnetic events), while short-term disturbances are largely suppressed by the integral. However, the definition of a proper baseline is required, since fluences are defined for events producing a finite input over a finite amount of time. Defining such baseline represents a major difficulty, because of relatively strong and sometimes uncorrelated $^{10}$Be/$^{9}$Be variations with typical ~20 ka duration, and different long-term quasi-linear trends, especially before the transition (Fig. 3a), as shown in Supplementary Fig. 2.

Quantitative comparisons therefore require a common baseline definition. This definition relies on matching all records over the two time intervals immediately preceding (808–853 ka) and following (707–743 ka) the M-B reversal, after applying a proper linear scaling to each of them. Rescaled $^{10}$Be/$^{9}$Be records are defined by

$$R_i' = (R_i - a_i') \,/\, b_i', \tag{1}$$

where $R_i'$ is the rescaled version of $R_i$ for core $i$ (see Table 2 for the core indices), and $a_i'$ and $b_i'$ are constant coefficients that minimize the squared differences between $R_i'$ and a reference record, chosen to be MD90-0961 due to its highest deposition rate. The use of additive coefficients $a_i'$ violates the assumption that the isotopic ratio is proportional to the global $^{10}$Be production rate; however, these coefficients are necessary to eliminate the large offsets seen in Fig. 3a. An overall good agreement is obtained for all $R_i'$ (Fig. 4a), which now share the same long-term trends outside the M-B reversal. A partial exception is represented by core MD95-2016 outside the 735–845 ka interval. The average of all rescaled profiles in Fig. 4a defines a common baseline $R_0'$, which can be subtracted from each $R_i'$ to obtain the net $^{10}$Be/$^{9}$Be increase during the M-B reversal. Different net increases are obtained for the five cores during the M-B reversal after rescaling (Fig. 4b), which means that the rescaling coefficients obtained with eq. (1) are not valid for the whole record duration. This is the first hint that points to different mechanisms controlling smaller variations during stable polarity intervals on the one hand, and major $^{10}$Be/$^{9}$Be increase during a geomagnetic event on the other. As it will be discussed in Section 5, these mechanisms are associated with climatic and geomagnetic modulations of the $^{10}$Be flux, respectively.

A second linear transformation is applied to the net rescaled enhancements $R_i' - R_0'$, this time using $a_i'' = 0$, since the baseline has been already subtracted, in order to collapse them onto the chosen reference. The final result is a set of normalized curves $\Delta R_i''$ (Fig. 4c), which are supposedly proportional to the $^{10}$Be flux increase during the M-B reversal. Residual differences between the rescaled records are nearly random and limited to short time intervals, mostly $< 10$ ka. A stacked record is then obtained by building an average $\Delta R''$ of all $\Delta R_i''$, except MD95-2016, which has a much larger variability unrelated to geomagnetic field changes. The good agreement between individual $\Delta R_i''$ reconstructions means that smoothing effects are likely absent, down to the ~10 ka duration of the precursor event at 795 ka. The lack of significant smoothing effects over the timescale of the M-B reversal is expected from the much shorter depth range of the Australasian tektite event (Supplementary Fig. 1) recorded just before the reversal (Valet et al., 2014).

The unnormalized total $^{10}Be/^{9}Be$ excesses caused by the M-B reversal is finally obtained by integrating $b_i' b_i'' \Delta R''(t)$ over time, with $b_i'$ and $b_i''$ being the multiplicative coefficients of the first and second scaling transformation, respectively. The $^{10}Be/^{9}Be$ fluence $\Delta R_{tot}$ of the M-B reversal was estimated using a trapezoidal integration of $^{10}Be/^{9}Be$ within the interval of 743–808 ka, which encloses the duration of the M-B reversal. $\Delta R_{tot}$ varies significantly among cores (Supplementary Fig. 2b), with the smallest and the largest values for MD95-2016 and MD98-2183, respectively. Moreover, $\Delta R_{tot}$ correlates significantly ($r^2 = 0.96$) with the water depth of the corresponding sites (except MD90-0961 for reasons explained later), but not with other parameters, such as sedimentation rate and calcium carbonate content. A similar correlation ($r^2 = 0.9$), with the same exception of core MD90-0961, is also found for the additive coefficients $a_i'$ used to rescale the baselines outside the M-B transition (Supplimentary Fig. 2b). Linear extrapolation of the observed dependence of $\Delta R_{tot}$ on water depth leads to the unlikely conclusion that $^{10}Be/^{9}Be$ variations during the M-B reversal drop to zero at water depths comprised between ~ 0.9 and 1.7 km. These observations are difficult to reconcile with modern dissolved $^{10}Be/^{9}Be$ profiles in the oceans (Kusakabe et al., 1990), which do not show a systematic increase below 1–2 km depth.

In summary, this preliminary analysis suggests that there are three distinct processes controlling the isotopic ratio: (1) the geomagnetic modulation, which dominates during the M-B reversal and is responsible for the observed peak at ~ 774 ka, (2) a different modulation, which is probably a mixture of geomagnetic and environmental effects, which controls small variations during periods of stable polarity, and (3) a site-specific, constant $^{10}Be$ flux providing a different baseline to each record. In the following sections these processes are analyzed with a modified version of the linear rescaling procedure illustrated above, which takes a common environmental modulation of $^{10}Be/^{9}Be$ into account.

## 5. The environmental modulation of $^{10}Be/^{9}Be$ records

As seen in section 4, there are strong evidences for a joint geomagnetic and environmental modulation of $^{10}Be/^{9}Be$ records during the M-B reversal. In the following, we analyse possible environmental modulation mechanisms and develop an empirical model that explains inter-core differences by a combination of climatic effects and scavenging of $^{10}Be$ reservoirs that are not synchronised with the global atmospheric $^{10}Be$ production rate (hereafter referred to as Be recycling).

### 5.1. Background

Particles suspended in ocean water containing dissolved beryllium grow an authigenic rim in which the so-called reactive Be concentration $C$ is related to the dissolved concentration $C_d$ by $C = C_d K_d$, where $K_d$ is the intrinsic solid-liquid partition coefficient of beryllium. The practically used bulk partition coefficient (Chase et al., 2002; Wittmann et al., 2017) differs from the intrinsic coefficient by the use of bulk solid concentrations, instead of rim concentrations, which makes it sensitive to grain sizes. The authigenic rim grows continuously, acquiring the isotopic composition of dissolved Be in water (Wittmann et al., 2017). In the following, it is assumed that the rim thickness increases at a rate λ while particles are in suspension. The bulk beryllium mass concentration accumulated on suspended matter when reaching the ocean floor is thus given by

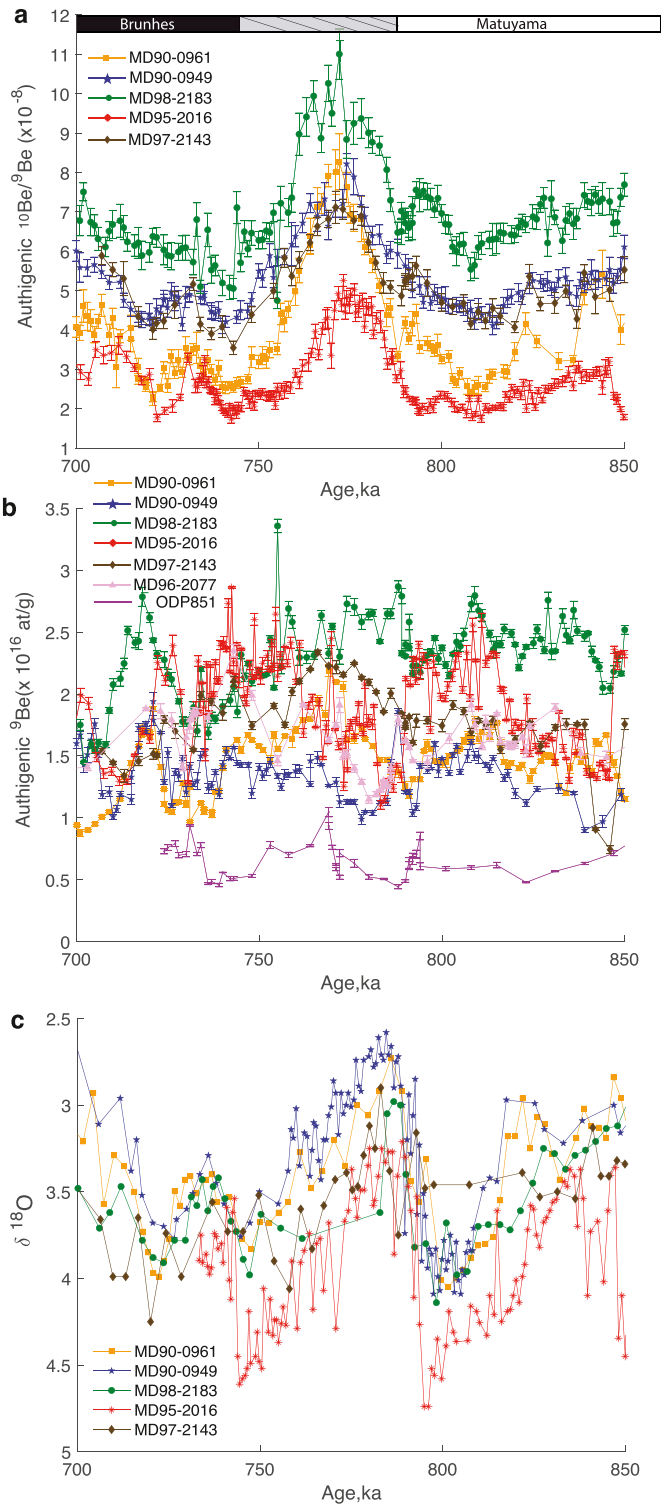


**Fig. 3.** **(a)** $^{10}Be/^{9}Be$ records tuned to match the age model of MD90-0961. **(b)** Same as (a) for $^{9}Be$ concentrations. **(c)** $\delta^{18}O$ records from planktonic foraminifera for the same cores as in (a).

$$C = \rho \int_0^T \lambda K_d C_d dt, \quad (2)$$

where $T$ is the residence time of particles in water, λ the accretion

rate of the authigenic rim (thickness per unit of time), and ρ the density of particles. Suspended matter can be divided into two pools: a pool of fine particles with negligible sinking velocity, which are carried by oceanic currents, and a pool of fewer, much larger, rapidly sinking particle aggregates (flocs), which are the effective scavenging carriers (McCave, 1975; Bacon et al., 1985). The same particle might be exchanged several times between a freely suspended, non-sinking state and a rapidly sinking aggregate, yielding a mean effective sinking velocity of 0.3–1 km/yr (Bacon et al., 1985), > 3 orders of magnitude less than the typical velocity of oceanic currents. Therefore, Be scavenging is strongly affected by lateral transport, so that the arguments of the integral in eq. (2) must be evaluated along paths $\Gamma(t, \mathbf{x}_0, T)$ of suspended particles from their starting points $\mathbf{x}_0$ at the ocean surface (in case of directly deposited dust) or along a coast (in case of continental provenance) to the sediment core location. Because several starting points are connected to the same endpoint, eq. (2) is integrated over all paths ending at the core location, obtaining

$$C = \rho \int_{\Omega} p(\mathbf{x}_0) \mathrm{d}\mathbf{x}_0 \int_0^T \lambda K_\mathrm{d} C_\mathrm{d}(\Gamma(t, \mathbf{x}_0, T)) \mathrm{d}t, \quad (3)$$

where $p(\mathbf{x}_0)$ is the probability of Γ, and Ω the "catchment"area of the core location. The ensemble of $p$ values corresponding to all combinations of start and endpoints defines the so-called surface-bottom transportation matrix (Nooteboom et al., 2019). The surface-ocean area Ω connected to the bottom is largest along large current systems, such as the western boundary currents (e.g. the Gulf Stream), because strong currents are often accompanied by eddies, which promote mixing. According to this model, sedimentary Be concentrations are affected by three main factors: (1) the uptake efficiency, expressed by λ and $K_\mathrm{d}$, (2) the dissolved Be concentration $C_\mathrm{d}$ along the settling paths Γ, and (3) the settling time $T$. The associated scavenging flux, which is obtained by multiplying $C$ with the vertical flux of suspended matter, removes dissolved Be from the water column. This effect is more pronounced at places with large sedimentary fluxes, for instance near the coasts, where it is known as boundary scavenging (Bacon, 1988; Anderson et al., 1990, 1994).

The isotope ratio $R$ obtained from the evaluation of eq. (3) for $^9$Be and $^{10}$Be is formally equivalent to a weighted average of the ratio $R_\mathrm{d}$ of dissolved isotopes along all settling paths Γ . All factors affecting Be concentrations will also affect isotopic ratios; however, some effects are greatly reduced. In particular, any time-dependent environmental modulation of $R$ requires inhomogeneous changes of $R_\mathrm{d}$ (horizontally, vertically, or both), or changes of the surface-bottom transportation matrix in areas with inhomogeneous isotope ratios, or both. Even in the ideal case of completely mixed oceanic basins, environmental effects arise from temporal changes of the $^{10}$Be or $^9$Be input fluxes, for instance through atmospheric precipitation patterns or continental denudation rates.

The geomagnetic modulation of $R$ depends only on $R_\mathrm{d}$, with a maximum delay controlled by the $^{10}$Be residence time in the water. Residence times are comprised between ~100 years at margin sites and ~3000 years at red-clay sites in the deep Central Pacific (Anderson et al., 1990). Sites with largest residence times might therefore produce significantly smoothed records of short geomagnetic events, such as excursion (Christl, 2007). The 200–700 year mean residence times of deep waters at the five sites investigated in this study (von Blanckenburg et al., 1996) are small compared to the duration of the M-B reversal. Because the smoothing effect associated with sediment mixing is also negligible over the timescale of the M-B reversal (Supplementary Fig.1), our $^{10}$Be/$^9$Be records are practically synchronous with geomagnetically induced variations of the cosmogenic production rate.

We now need to link $R_\mathrm{d}$ with the $^{10}$Be production rate. Assuming rapid and complete mixing of authigenic Be, von Blanckenburg and Bouchez (2014) modeled dissolved $^{10}$Be/$^9$Be values in terms of oceanic mass balance. If atmospheric fluxes of $^{10}$Be intercepted by rivers and directly by the ocean are written as $F_\mathrm{riv}^{10} = \phi_\mathrm{riv} P$ and $F_\mathrm{oc}^{10} = \phi_\mathrm{oc} P$, respectively, with $\phi_\mathrm{riv}$ and $\phi_\mathrm{oc}$ being the corresponding efficiencies of atmospheric $^{10}$Be scavenging to the oceans and to the river basins, respectively, and $P$ the global cosmogenic production rate, the ratio of dissolved isotopes derived by von Blanckenburg and Bouchez (2014) can be written as

$$R_\mathrm{d} = \frac{\left(A^\mathrm{oc} / A^\mathrm{riv}\right)\phi^\mathrm{oc} + \phi^\mathrm{del}\phi^\mathrm{riv}}{\phi^\mathrm{del} D^\mathrm{riv} C_9^\mathrm{rock}\left(f_9^\mathrm{reac} + f_9^\mathrm{diss}\right)} P, \quad (4)$$

where $A^\mathrm{oc}$ and $A^\mathrm{riv}$ are the total areas of the oceans and river watersheds, respectively, $\phi^\mathrm{del}$ is the efficiency of overall riverine Be delivery to the ocean, $D^\mathrm{riv}$ is the average denudation rate in the basins drained by rivers, $C_9^\mathrm{rock}$ is the mean $^9$Be concentration in parent rocks delivering eroded material to the river, and $f_9^\mathrm{reac} + f_9^\mathrm{diss}$ the fraction of $^9$Be released during weathering from the parent rock, either in reactive phases or dissolved. It is clear from eq. (4) that the environmental modulation of $R_\mathrm{d}$ is purely multiplicative.

In the more realistic case of incomplete basin mixing, expressions similar to eq. (4) might be applied to smaller pools, or to poorly mixed water masses (e.g. deep waters), with boundary conditions given by the exchange rates of dissolved Be between pools. The direct proportionality relation between $R_\mathrm{d}$ and $P$ is thereby maintained, as long as the mean Be residence time of all

**Table 2**
Summary of model parameters corresponding to solution 14 (Fig. 6d). $A$ and $B$ are the additive and multiplicative coefficients of eq. (11) with core MD95-2016 as a reference, and $\delta A$ and $\delta B$ the corresponding variations about the time averages $\langle A \rangle$ and $\langle B \rangle$, respectively.$^{10}$Be/$^9$Be values at the surface of ferromanganese crusts collected at nearest sites (from Von Blanckenburg et al., 1996) and$^{10}$Be/$^9$Be values obtained by normalizing the modern atmospheric$^{10}$Be flux at the core sites (from Deng et al., 2020) with the sedimentary $^9$Be flux for the same sites are listed for comparison. The coefficients $A$ and $B$ for sites indicated in italics have been obtained assuming that they are constant over time.

| index | core | $\langle -\mathbf{A} \rangle$ | $\max(\delta\mathbf{A})$ | $\langle 1/\mathbf{B} \rangle$ | $\max(\delta(1/\mathbf{B}))$ | $(^{10}\mathbf{Be}/^{9}\mathbf{Be})_\mathrm{FeMn}$ | $(^{10}\mathbf{Be}/^{9}\mathbf{Be})_\mathrm{at}$ |
|---|---|---|---|---|---|---|---|
| | | $10^{-8}$ | $10^{-8}$ | | | $10^{-8}$ | $10^{-8}$ |
| 1 | MD98-2183 | 2.37 | 0.21 | 1.43 | 0.12 | 13.0 | 3.14 |
| 2 | MD97-2143 | 2.17 | 0.37 | 1.07 | 0.13 | 10.0 | 4.10 |
| 3 | MD90-0949 | 2.99 | 0.18 | 0.92 | 0.11 | 8.8 | 7.97 |
| 4 | MD90-0961 | 0.11 | 0.79 | 1.50 | 0.26 | 7.1 | 4.37 |
| 5 | MD95-2016 | 0.00 | – | 1.00 | – | 3.9 | 3.37 |
| _ | *MD05-2930* | 0.06 | – | 0.77 | – | – | 0.96 |
| _ | *Chiba* | 0 | – | 0.56 | – | – | 0.09 |

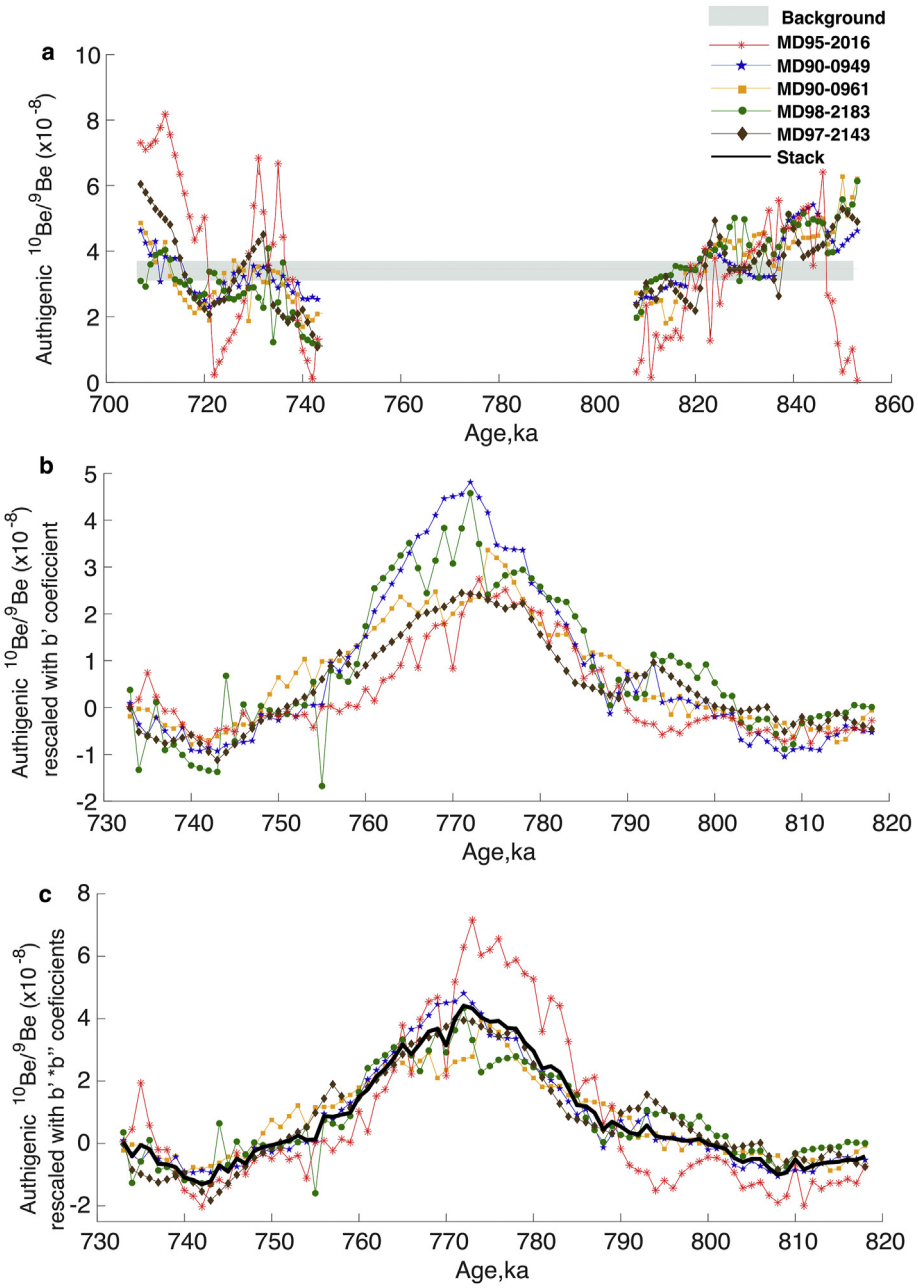


**Fig. 4.** **(a)** Linearly scaled $^{10}$Be/$^{9}$Be records adjusted to match core MD90-0961 outside the M-B interval. The thick gray line represents the mean offset of all records, except MD95-2016. **(b)** The same linear rescaling procedure used in (a) is now applied to the M-B interval, after removing the mean offset. **(c)** Stack obtained from (b) after a second rescaling step used to remove the residual differences with respect to core MD90-0961. The thick black line is the average of all rescaled records, except MD95-2016.

pools remain small compared to the timescale of geomagnetic variations. A similar conclusion is valid for the relation between $R$ and $R_d$ derived from eq. (4). With these assumptions in place, combination of eqs. (3) and (4) yields a result of the form $R = \beta_d \beta_s P$, where $\beta_d$ and $\beta_s$ are site- and time-dependent factors expressing the environmental modulation of $R_d$ (eq. (4)) and of the scavenging flux (eq. (3)), respectively. This result supports current geomagnetic dipole reconstruction techniques based on the normalization of $R$ with a calibration constant $R_0$, which is chosen by matching $R/R_0$ with the global $^{10}$Be production rate expected at a reference time with known VADM (e.g. Simon et al., 2016a, 2018a,b). However, as discussed in Section 4, certain differences between $^{10}$Be/$^{9}$Be records of the M-B reversal that can only be explained by the existence of a nearly constant, site-specific offset, which can be as large as the geomagnetic modulation caused by the reversal itself. This offset does not prevent the stratigraphic identification of the $^{10}$Be increase associated with major geomagnetic events, but questions the accuracy of inter-core calibrations.

In summary, $^{10}$Be/$^{9}$Be records are independently controlled by five main variables: (1) the cosmogenic $^{10}$Be production rate, which depends on the geomagnetic dipole moment, (2) the distribution of surficial Be sources (atmospheric scavenging, dust fluxes, riverine inputs, melting ice masses), (3) scavenging of old Be reservoirs (Be recycling), (4) oceanic circulation (advective transport, mixing), and (5) sedimentary fluxes. Variables 2–4 affect $\beta_d$, while $\beta_s$ depens on variables 4–5. The complex interplay between these variables is

controlled mainly by the distance from the coast and by large current systems across ocean basins, as exemplified for the South Atlantic (Measures et al., 1996).

### 5.2. Reconstruction of the environmental modulation

Additive and multiplicative environmental effects of individual $^{10}Be/^{9}Be$ records cannot be reconstructed without an independent estimate of the cosmogenic $^{10}Be$ flux. Here we propose a possible strategy to overcome this limit by disentangling geomagnetic and environmental contributions to several records of the same event, in this case the M-B reversal. Following the preliminary profile processing discussed in Section 4, we consider pairs of $^{10}Be/^{9}Be$ records $R_i$ and $R_j$ at sites $i$ and $j$, respectively, and model the differences introduced by environmental effects using a linear transformation to rescale $R_j$ so that it becomes equal to $R_i$:

$$R_i(t) = A_{ij} + B_{ij}R_j(t), \tag{5}$$

where $A_{ij}$ and $B_{ij}$ are site-specific functions representing the additive and multiplicative environmental modulation of site $j$ relative to site $i$. Solution of eq. (5) with respect to $R_j$ yields

$$R_j(t) = A_{ji} + B_{ji}R_i(t) = \frac{R_i(t) - A_{ij}}{B_{ij}}, \tag{6}$$

so that the reciprocal relations $A_{ji} = -A_{ij}/B_{ij}$ and $B_{ji} = B_{ij}^{-1}$ hold between the coefficients. Environmental changes make these coefficients depend on time. In case of global climatic responses, they can be assumed to be functions of a common global climate proxy $S(t-t_0)$ , such as $\delta^{18}O$, where $t_0$ is a time lag accounting for a delayed or anticipated response of the beryllium signal modulation with respect to $S$ (e.g. Tuenter et al., 2005). The dependency of $A_{ij}$ and $B_{ij}$ on $S$ must be small, for beryllium records to be a useful proxy of cosmogenic production. Therefore, the first two terms of the Taylor series of $A_{ij}(S)$ and $B_{ij}(S)$ should adequately represent the global environment modulation. In this case we can write

$$\begin{aligned} A_{ij}(t) &= a_{ij}^0 + a_{ij}^1 S\left(t - t_{ij}^a\right) + \varepsilon_{ij}^a(t) \\ B_{ij}(t) &= b_{ij}^0 + b_{ij}^1 S\left(t - t_{ij}^b\right) + \varepsilon_{ij}^b(t) \end{aligned} \tag{7}$$

where $a_{ij}^{0,1}$ , $b_{ij}^{0,1}$ are the first two Taylor coefficients of $A_{ij}(S)$ and $B_{ij}(S)$, respectively, $t_{ij}^a$ and $t_{ij}^b$ are the time lags of additive and multiplicative modulations, and $\varepsilon_{ij}^a$, $\varepsilon_{ij}^b$ are additional functions representing environmental effects that do not correlate with $S(t)$, which can be effectively treated as a noise source.

Solutions for the coefficients $a_{ij}^{0,1}$ and $b_{ij}^{0,1}$ for a given set of records can be found by minimizing the sum of squared differences between measured values of $R$ and reconstructed values using eq. (7), with constraints given by the reciprocity relations for $j > i$ (eq. (6)). We intentionally neglect $\varepsilon_{ij}^a$ and $\varepsilon_{ij}^b$ to obtain the meaningful solutions, because environmental effects not accountable by $S(t)$ must be small, or cover a frequency range that does not overlap with $S$ or the geomagnetic modulation. The scaling coefficients in eq. (7) are linear with respect to $a_{ij}$ and $b_{ij}$, but not with respect to the time lags $t_{ij}^a$ and $t_{ij}^b$, due to the quasi-periodic character of the climatic proxy $S$. Therefore, distinct solutions might be obtained from different initial choices of $t_{ij}^a$ and $t_{ij}^b$. In the following model implementation, the global climatic signal is identified with the mean $\delta^{18}O$ record of the Indian Ocean cores MD90-0949 and MD90-0961 (Fig. 5), which matches the glacial-interglacial sawtooth pattern of benthic $\delta^{18}O$ stacks (Lisiecki and Raymo, 2005). Our choice of a single climatic proxy might not be flexible enough to account for selective responses to individual forcing parameters, such as that of the thermohaline circulation to the obliquity band (Brickman et al., 1999; Antico et al., 2010). In this case, residual differences between records might direct the choice of more suited proxies of $S$.

A least-squares collocation algorithm (Moritz, 1978) is used to produce a smoothed interpolation of the original $\delta^{18}O$ record, which is identified with the climatic function $S(t)$ (Fig. 5b). Least-squares collocation is particularly suited for the interpolation of irregularly sampled, noisy signals, and it is used here also to obtain slightly smoothed versions of the $^{10}Be/^{9}Be$ records of all cores between 715 and 830 ka. This interval includes the whole period of enhanced $^{10}Be$ production associated with the M-B field reversal, and ~30 ka before and after. The use of smoothed records facilitates the solution convergence. Initial parameters are chosen to reproduce the case of no climatic modulation, that is $a_{ij}^0 = a_{ij}^1 = 0$ (no additive effects), $b_{ij}^0 = 1$ (same responses at all sites), and $b_{ij}^1 = 0$ (no multiplicative effects). Initial $t_{ij}^a$ and $t_{ij}^b$ values were comprised between ±20 ka, which is about 1/4 of the main period of $S(t)$.

As seen in Fig. 6, our climatic modulation model produces an almost perfect match between rescaled records over the selected 715–830 ka interval. Few residual differences can be seen for the North Atlantic core MD95-2016, but the overall agreement is generally better than the random scatter of individual records. This means that a single climatic function is sufficient to explain all significant differences between the records. Solution multiplicity is due to the limited redundancy of eq. (7): the most evident common features of the five records can be represented with 11 points (arrows in Fig. 6a), yielding a total of 110 independent $^{10}Be/^{9}Be$ differences between profiles, which are fitted using 60 model parameters. The goodness of each solution can be evaluated by comparing the original records with reconstructions obtained from stacks of rescaled records. For this purpose, a reference core is chosen (e.g., MD95-2016 as in Fig. 6c–d), and the other records are rescaled to match this reference using the coefficients of a given solution (e.g., solution 14 in Fig. 6d). The reference core selection is arbitrary, since every solution contains the coefficients required to transform any record into any other record. Our choice of MD95-2016 ($i$ = 5, Table 2) for displaying the model results is based essentially on the fact that it is the record with the smallest absolute offset, as seen from the fact that $a_{5j} \leq 0$ for all $j$.

A stack matching the chosen reference core is then constructed by averaging the rescaled records. This operation reduces the random scatter produced by noise and local environmental effects unaccountable by the common climate signal $S$. Finally, this stack is rescaled with eq. (6) to match each of the other four cores, producing a set of reconstructed records (solid lines in Fig. 7) that are entirely explainable by a global climatic modulation of the cosmogenic $^{10}Be$ production rate. Model residuals, given by the differences between measured and reconstructed records, contain noise and local environmental effects that are not captured by the chosen global climatic proxy $S$. These residuals are smaller, on average, than noise contributions in individual records. This result validates the initial assumption that environmentally-driven differences between records can be almost entirely explained by global climatic variations recorded by benthic $\delta^{18}O$.

The obtained model solutions can be divided into three main groups with distinct time dependencies of $A_{ij}$ and $B_{ij}$. The first group (Fig. 8a) is characterized by unrealistically large, strongly

anti-correlated time variations of $A_{ij}$ and $B_{ij}$. An implausibly fine-tuned cancellation of the opposite trends produced by the additive and multiplicative coefficients yields an environmental modulation that is very dissimilar to $S(t)$. The existence of a strong correlation between $A_{ij}$ and $B_{ij}$ is unreasonable, because of the distinct physical origin of additive and multiplicative environmental effects. This group of solutions is therefore discarded.

Additive and multiplicative coefficients of the second solution group display much smaller temporal variations, with all $A_{ij}$ being in-phase with $S$, and all $B_{ij}$ being lagged by 25–30 ka (Fig. 8b). The combined effect of additive and multiplicative coefficients result in an oscillatory modulation of all records relative to the North Atlantic core MD95-2016, whose ~40 ka main period does not reflect glacial-interglacial cycles. The large temporal offset of the multiplicative coefficients of the second solution group with respect to $\delta^{18}$O implies a ~28 ka-delayed response to the MIS 20 glaciation, which is difficult to explain. For instance, numerical oceanic circulation models predict a maximum lag of ~ 10 ka for the Atlantic Ocean thermohaline circulation with respect to precession and obliquity bands (Tuenter et al., 2005). Furthermore, the relatively large temporal modulation of the additive coefficients in this solution group implies that recycled $^{10}$Be inputs at the MD95-2016 site increased during the MIS 20 glacial, relative to the other cores. There are two likely sources of recycled $^{10}$Be in the North Atlantic (1) meltwater impulses from large ice-sheets (e.g. Simon et al., 2016) and (2) the Antarctic Bottom Water (AABW), which might have been enriched with diagenetic $^{10}$Be releases from the seafloor. In the first case, Be recycling is expected to occur after the Termination IX. In the second case, the northern AABW limit is expected to expand during glacial times (Ferrari et al., 2014), but not as far as to reach the MD95-2016 site if the last glacial maximum (LGM) is used as a MIS 20 analogue (Seidov et al., 1996; Paul and Schäfer-Neth, 2003). Therefore, the environmental modulation predicted by the second solution group is also implausible, leaving the third group as the only candidate with a physical meaning.

The third solution group is characterized by nearly constant additive coefficients (with the moderate exception of core MD90-0961), while the multiplicative coefficients generate small temporal variations that are in-phase with respect to $S$ (Fig. 8c). The physical meaning of this solution group is discussed in the following.

### 5.3. Solution evaluation

Plausible solutions for our model (Fig. 8c) yield multiplicative environmental modulations that depend on glacial-interglacial cycles, with all cores showing very similar temporal changes relative to the North Atlantic site MD95-2016. These changes can be explained by a $^{10}$Be concentration increase or a diagenetic $^{9}$Be concentration decrease in MD95-2016, relative to all other cores, during the MIS 20 glaciation. Global oceanic circulation models (Seidov et al., 1996; Paul and Schäfer-Neth, 2003) indicate that MD95-2016 is located close to the northern limit of an anticlockwise gyre fed by the North Atlantic Drift (NAD). A sediment particle sinking at the MD95-2016 site would first cross this gyre and then the return path feeding the North Atlantic deep water (NADW). The isotopic ratio of this conveyor belt current system is dominated by the uptake of $^{10}$Be-rich precipitations at mid-latitudes, along the western North Atlantic path of the Gulf stream (Heikillä and Smith, 2013; Cao et al., 2019; Deng et al., 2020). Little or no currents are predicted at this site below ~2 km depth, so that the NAD can be regarded as the main source of non-recycled $^{10}$Be.

Following the scavenging model discussed in Section 5.1, we assume that the multiplicative environmental modulation of MD95-2016 is composed of an oceanic term that is mainly controlled by the efficiency with which the NAD transports $^{10}$Be from mid latitudes, and an atmospheric term mainly controlled by mid-latitude atmospheric precipitations over the Western Atlantic. Global oceanic circulation models suggest a slight decrease of superficial currents during the last glacial maximum (LGM) (Seidov et al., 1996; Paul and Schäfer-Neth, 2003). Moreover, mid-latitude precipitations over the NW Atlantic are also predicted to decrease during glacials (Cao et al., 2019), so that a decrease of dissolved $^{10}$Be concentration is expected during the MIS 20 glaciation at the MD95-2016 site. This contradicts the trend suggested by the $B_{ij}$ coefficients, unless it is assumed that a similar, but stronger modulation occurs in the other cores. On the other hand, less chemical weathering, and therefore less diagenetic $^{9}$Be production is expected during glacial times at high latitudes. Caution should be used with the identification of sedimentary $^{9}$Be concentrations (Fig. 3b) with dissolved values, because of possible variations caused by changes of the scavenging efficiency or of the $^{9}$Be delivery. Nevertheless, MD95-2016 is affected by the largest $^{9}$Be variations, with a marked drop at ~780 ka, just before the MIS 20 termination. It is, therefore, possible that the distinct climatic modulation of $^{10}$Be/$^{9}$Be at MD95-2016 is due to relatively large $^{9}$Be input variations that are negatively correlated with benthic $\delta^{18}$O (Fig. 3).

As far as the additive coefficients are concerned, our model predicts large, almost constant differences between cores, which can be effectively regarded as fixed site-specific offsets. All coefficients are negative with respect to MD95-2016, which means that MD95-2016 has the smallest absolute offset. The absolute offset of MD95-2016 must be negligibly small, because the maximum $^{10}$Be/$^{9}$Be increase of during the M-B reversal is only slightly smaller than the ~2.2× maximum increase predicted by cosmogenic production models for the disappearance of the dipole field (Heikillä et al., 2009; Poulianov et al., 2016; Simon et al., 2018b). Accordingly, the coefficients $-A_{5,j}$ (Table 2) can be identified with the absolute offset of each site. The most affected core is MD90-0949, with an offset of $\sim 3 \times 10^{-8}$, corresponding to ~60% of the average $^{10}$Be/$^{9}$Be level outside the M-B reversal. A similar offset is obtained for MD97-2143, while MD90-0961 has only a small offset, which, however, is less constant in time. Overall, 40–60% of the isotopic ratio of three cores from the Pacific and the Indian Ocean is controlled by a constant $^{10}$Be input unrelated to the cosmogenic production rate. As discussed in Section 4.1, constant offsets can be subtracted without altering the production rate-dependent component of $^{10}$Be/$^{9}$Be records.

The above discussion demonstrates the complex nature of the environmental modulation of beryllium records. Site-specific differences are controlled by additive and multiplicative processes. The additive component is relatively constant in time, so that the environmental modulation depends ultimately on the evolution of the product of atmospheric and oceanic scavenging efficiencies. Accordingly, atmospheric and oceanic responses to solar forcing are combined in a multiplicative manner. Oceanic convection is most sensitive to obliquity (~40 ka cycles) and rectified precessional forcing (~20 ka cycles), while the atmosphere is controlled by the solar radiation, with most power being concentrated in the obliquity and eccentricity bands (~100 and ~400 ka cycles) (Brickman et al., 1999; Antico et al., 2010; Schmittner and Clement, 2002). Contributions from the ~20 ka band could be responsible for the residual discrepancies between rescaled $^{10}$Be/$^{9}$Be records at 700–740 ka and 860–880 ka (Fig. 6). The remaining discussion of our model results focuses on site-specific effects, which are expressed by the time averages of $A_{ij}$ and $B_{ij}$ coefficients. Results from a $^{10}$Be/$^{9}$Be record of the M-B reversal obtained from core MD05-2930 (Ménabréaz et al., 2014) and from the Chiba composite

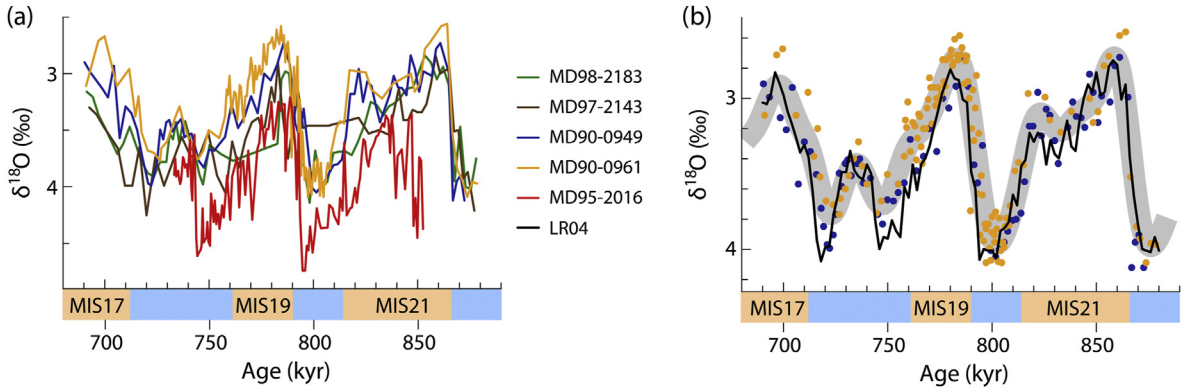


**Fig. 5.** **(a)** Measured benthic $\delta^{18}$O records over a time interval that includes the M-B reversal. **(b)** Least-squares collocation fit (thick gray line) of the benthic $\delta^{18}$O records of MD90-0949 (blue dots) and MD90-0961 (yellow dots). The benthic $\delta^{18}$O stack LR04 (Lisiecki and Raymo, 2005) is shown for comparison (black line) after subtracting a constant offset of 0.75. (For interpretation of the references to colour in this figure legend, the reader is referred to the Web version of this article.)

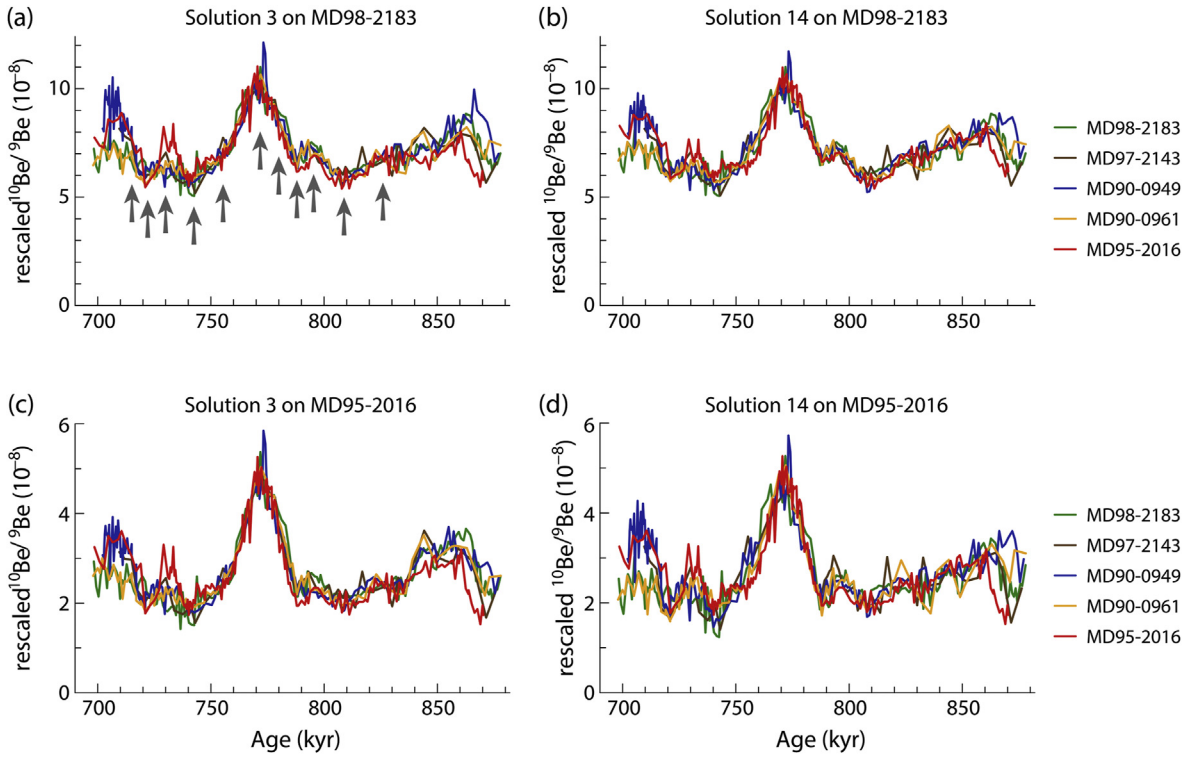


**Fig. 6.** Examples of $^{10}$Be/$^{9}$Be profiles rescaled according to eqs. (5)–(7) and the climatic function of Fig. 5b, for best match with MD98-2183 **(a–b)** and MD95-2016 **(c–d)**. Left and right plots show the results for two of the 14 solutions that minimize the mean squared differences between rescaled profiles. Arrows in (a) point to specific features (main peak, local minima and maxima) that have been matched by the rescaling procedure.

section (Simon et al., 2019) are included for comparison. Please note that the *A* and *B* coefficients of these cores have been assumed to be constant in time (Table 2).

## 6. Discussion

### 6.1. The origin of sedimentary $^{10}$Be

As seen in Section 4, $^{10}$Be/$^{9}$Be records of the M-B reversal can be decomposed into two independent components related to the coefficients *A* and *B* required to describe the observed differences between sites. The first component reproduces the expected geomagnetic modulation of the cosmogenic $^{10}$Be production rate with a site-specific proportionality constant $1/B$. The second component, nearly equal to $-A$, represents a site-specific, positive and nearly constant offset of $^{10}$Be/$^{9}$Be, which is unrelated to the cosmogenic $^{10}$Be production rate. In the following, we refer to these terms as the synchronous component and the offset of the $^{10}$Be/$^{9}$Be record, respectively.

The synchronous component is slightly delayed by the residence time of $^{10}$Be in the ocean, which is of the order of 1000 years or less at our sites (Raisbeck et al., 1980; Von Blanckenburg et al., 1996; Koeve et al., 2015). A further delay and smoothing is introduced by sediment mixing (Christl, 2007), whose time scale is given by $T_{mix} = L/v_s$, where *L* is the thickness of the mixed layer, and $v_s$ the deposition rate of sediment (Guinasso and Schink, 1975). Using

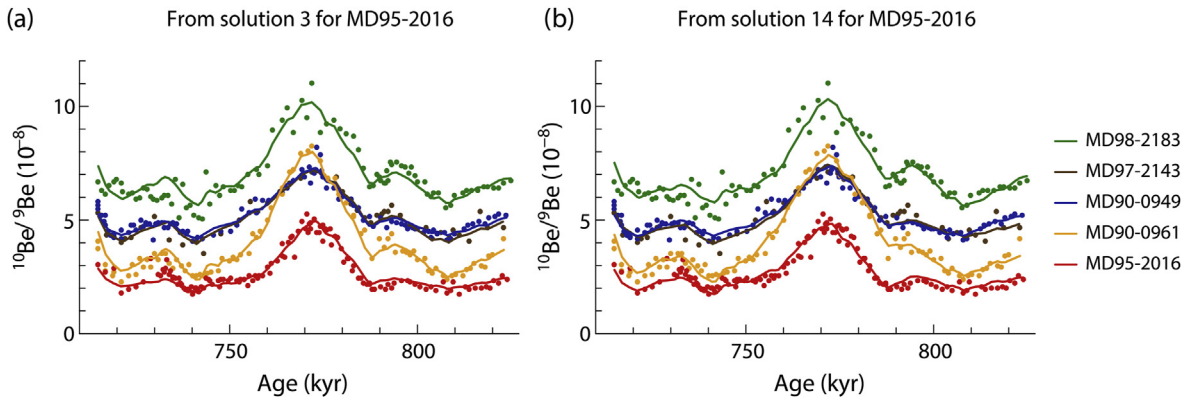


**Fig. 7.** $^{10}Be/^{9}Be$ measurements (dots), and reconstructed profiles from solution 3 **(a)** and solution 14 **(b)** of the rescaling algorithm. The reconstruction involves two steps: first, rescaling of all profiles with eqs. (5)–(7) to match MD95-2016; second, creation of a stack. This stack is then rescaled to match each of the five records, using the inverse transformation given by eq. (6) (lines). Differences between reconstructed records and measurements are entirely controlled by the climatic signal $S(t)$ and the model parameters.

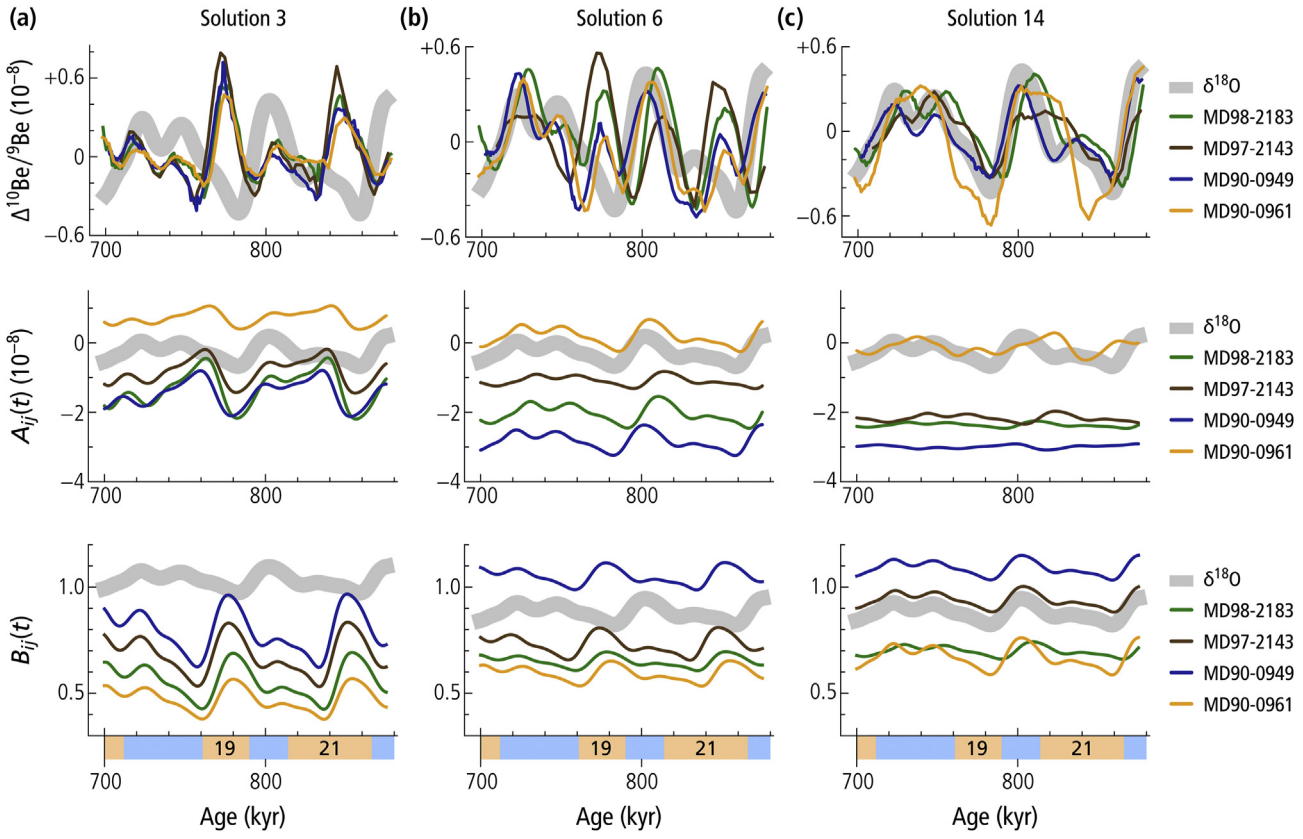


**Fig. 8.** Total (first row), additive (second row) and multiplicative (third row) environmental modulation of $^{10}Be/^{9}Be$ relative to MD95-2016, predicted by three solution groups. Additive and multiplicative modulations are defined by the coefficients $A_{ij}$ and $B_{ij}$ , respectively, with $i$ corresponding to the reference core MD95-2016. The total modulation is defined as the difference between rescaled profiles obtained with original and time-averaged coefficients, respectively. A rescaled version of the climatic modulation function ($\delta^{18}O$) is shown with thick gray lines for comparison.

$L \approx 10$ cm (Boudreau, 1998; Solan et al., 2019) and $v_s$ values from Table 1, we obtain $T_{mix} \leq 8.3$ ka for our cores. These estimates are independently confirmed by the thickness of the microtektite layer found in the two Indian Ocean cores (Supplementary Fig. 1). Sediment mixing is therefore not expected to introduce significant smoothing artifacts at the time scale of the M-B reversal. Delay and smoothing of the synchronous component can be minimized with the choice of cores with large deposition rates, enabling the record of much shorter geomagnetic events, such as the Iceland Basin excursion (~190 ka, <5 ka duration) (Knudsen et al., 2008).

The constant offsets, on the other hand, point to $^{10}Be$ inputs that are not affected by changes of the cosmogenic production rate. For this to be possible, the corresponding age distribution needs to largely exceed the ~30 ka total duration of the M-B reversal, so that the associated increase of the cosmogenic production rate remains unnoticeable. The two components cannot be distinguished during periods of regular dipole field intensity, because the isotope composition associated with synchronous $^{10}Be$ inputs at a given

site is undistinguishable from the long-term average responsible for the offset. Only the analysis of a time interval characterized by large changes of the cosmogenic production rate, such as during the M-B reversal, enables discrimination between the synchronous component and the offset. The relations observed between the *A* coefficients and other site parameters (Fig. 9) provide additional information about the nature of the offset. For instance, the absence of a significant offset for the North Atlantic site MD95-2016 excludes recycled $^{10}$Be sources related to ice-sheet melting, as in the case of more closed basins like the Baffin Bay (Simon et al., 2016b). This restricts the choice to (1) sources of ancient $^{10}$Be (e.g., terrigenous) or (2) post-depositional processes causing a partial remobilization of beryllium in the sedimentary column, over distances largely exceeding the mixing depth. The compatibility of these two offset sources with other site characteristics is discussed in the following.

*Terrigenous inputs*—Terrigenous inputs capable to produce the observed constant offsets must have a sufficiently wide $^{10}$Be age distribution to completely erase the geomagnetic variations. Simulated responses to the M-B reversal originating from lognormal age distributions require these distribution to extend over $>100$ ka to flatten the signal within the uncertainty of our model residuals, which are of the order of $\sim 1\times10^{-8}$ (Supplementary Fig. 3). These distributions are compatible with surface ages of weathering soils (Maher and Von Blanckenburg, 2016) and can explain the existence of a constant offset provided by the inner authigenic rim of sediment particles that preserves the $^{10}$Be/$^{9}$Be characteristics of continental erosion. In this case, the sedimentary $^{10}$Be/$^{9}$Be ratio can be written as

$$R_{sed}=\frac{F_{10}^{terr}+F_{10}^{atm}}{F_{9}^{terr}}=\frac{F_{10}^{terr}}{F_{9}^{terr}}+\frac{F_{10}^{atm}}{F_{9}^{terr}} \quad (8)$$

where $F^{terr}$ is the authigenic Be flux from terrigenous inputs (via rivers and dust), and $F_{10}^{atm}$ the flux of meteoric $^{10}$Be at the site. If the observed $^{10}$Be/$^{9}$Be offset is entirely of terrestrial origin, it is contained in the first term on the right-hand side of eq. (8), while the second term accounts for the synchronous component of the record. In this case, however, $^{10}$Be/$^{9}$Be values of $\sim 5\times10^{-9}$ or less typical of rivers and terrigenous sediments (Wittmann et al., 2015, 2017; Dhal et al., 2018) are largely insufficient to explain the observed offsets of $>2\times10^{-8}$ in the three deepest cores. Furthermore, eq. (8) predicts that the offset caused by terrigenous sources would entirely reflect the characteristics of these sources rather than those of the site. Increasing the distance from the coast is expected to decrease the sedimentary flux, lowering $F_{10}^{terr}$ and $F_{9}^{terr}$ by the same factor, so that the ratio represented by the first right-hand side term of eq. (8), and thus *A*, remains unchanged. Instead, the observed offsets and $^{10}$Be/$^{9}$Be values of ferromanganese crusts from nearby sites appear to be strongly controlled by water depth (Fig. 9a and b). The isotope composition of these crusts in turn reflects that of deep ocean waters (von Blanckenburg et al., 1996).

*Diagenetic Be mobilization*—Partial mobilization of authigenic beryllium in the sedimentary column might explain the partition of the $^{10}$Be/$^{9}$Be signal record into the two components described above. The synchronous component would be carried by the fractions of $^{9}$Be and $^{10}$Be that are irreversibly adsorbed on sediment particles, while the offset component requires a vertical transport of exchangeable Be capable of mixing a sufficiently large interval of ages, which, in our case, corresponds to several meters covered by the M-B reversal. As discussed for the terrigenous input hypothesis, mixing over age intervals largely exceeding the typical duration of geomagnetic events produces a mean isotope ratio of the mobilized phases close to that of periods with normal geomagnetic dipole intensity. Mobilized Be can be either redistributed within the sedimentary column, or released to the bottom water, in which case it is scavenged by settling particles and returned to the sediment. Scavenging of Be released into bottom waters by reductive dissolution of Fe- and Mn-oxyhydroxides, which adsorb a significant fraction (50–80%) of the extractable authigenic Be fraction (Bourlès et al., 1989a), was postulated by Wittmann et al. (2017). Reductive diagenesis in the oxic and suboxic environments typical of our cores occurs in the uppermost few tens of cm of the sedimentary column (Buridge, 1993; Elrod et al., 2004; Staubwasser et al., 2006). The maximum age of Be associated with Fe and Mn minerals dissolved at depths $<30$ cm, which is of the order of 15–20 ka for the three cores with a significant $^{10}$Be/$^{9}$Be offset (Tables 1–2), would be sufficient to smooth the M-B record, but cannot explain a constant offset over the ~150 ka range of our records. It is also interesting to observe that the few existing estimates of $^{9}$Be fluxes from sediment to the water column, which are of the order of 1 nmol/cm$^2$ka (Measures and Edmond, 1982; Bourlès et al., 1989b) represent 1–2.4% of the sedimentary $^{9}$Be fluxes in our cores and are also insufficient to explain the 30–50% recycled Be inputs outside the M-B reversal deducible from our largest *A* coefficients.

Higher recycled Be fluxes can be explained by assuming that most recycled Be originates at different sites, for instance in areas of the Central Pacific with very low sedimentation rates, and is then transported to marginal sites by bottom water currents. Vast regions of the Central Pacific with deposition rates of 0.1 cm/ka or less (Piper and Williamson, 1977) can be the source of Be release from the reductive diagenesis of Fe- and Mn oxyhydroxides at $<30$ cm. In this case, the $<150$ ka age range of the source sediment and its authigenic Be would be sufficiently large to explain a constant offset at distant sites where the released Be is scavenged.

Be mobilization within the sedimentary column is also made possible by other diagenetic mechanisms. For instance, the unstable Fe-oxyhydroxide ferrihydrite is transformed into thermodynamically stable hematite under fully oxic conditions via a two-stage recrystallization process involving goethite as intermediary product (Das et al., 2011). The first-order reaction rate $k\approx 0.01$ ka$^{-1}$ at 2 °C extrapolated from experiments at higher temperatures (Walter et al., 2001) would be of the right order of magnitude to explain the release of Be from $>100$ ka old sediment. Other diagenetic mechanisms include carbonate recrystallization, which commonly occurs during sediment compaction over depths of several tens of meters, even in the absence of net dissolution (Fantle et al., 2010). This process controls the reactive transport of elements that adsorb/desorb on $CaCO_3$, such as Sr (Richter and DePaolo, 1987; Fantle and DePaolo, 2007). Calcium carbonate contributes to phase II in the Be extraction procedure of Bourlès et al. (1989a), which represents 20–50% of the authigenic Be content of sediments. Finally, biogenic silica dissolution can also contribute to a significant Be release over a wide range of sediment ages, both directly (up to 20%, Bourlès et al., 1989a), and indirectly through the concomitant dissolution of iron oxides by silicic acid (Florindo et al., 2003).

In summary, ancient Be can be released to the water column from labile phases subjected to reductive diagenesis at sites with sufficiently small deposition rates, or redistributed over large distances in the sedimentary column through burial diagenesis. Both mechanisms can explain the observed $^{10}$Be/$^{9}$Be offsets. The stepwise dependence of the *A* coefficients on water depth displays a critical threshold of 2.5–2.9 km (Fig. 9a). This threshold coincides with the modern calcite saturation depth at the individual core locations (Feely et al., 2004; Gehlen et al., 2007), below which net calcite dissolution begins (Subhas et al., 2015), and also with the upper limit of deep water circulation in the Pacific (Rippert et al.,

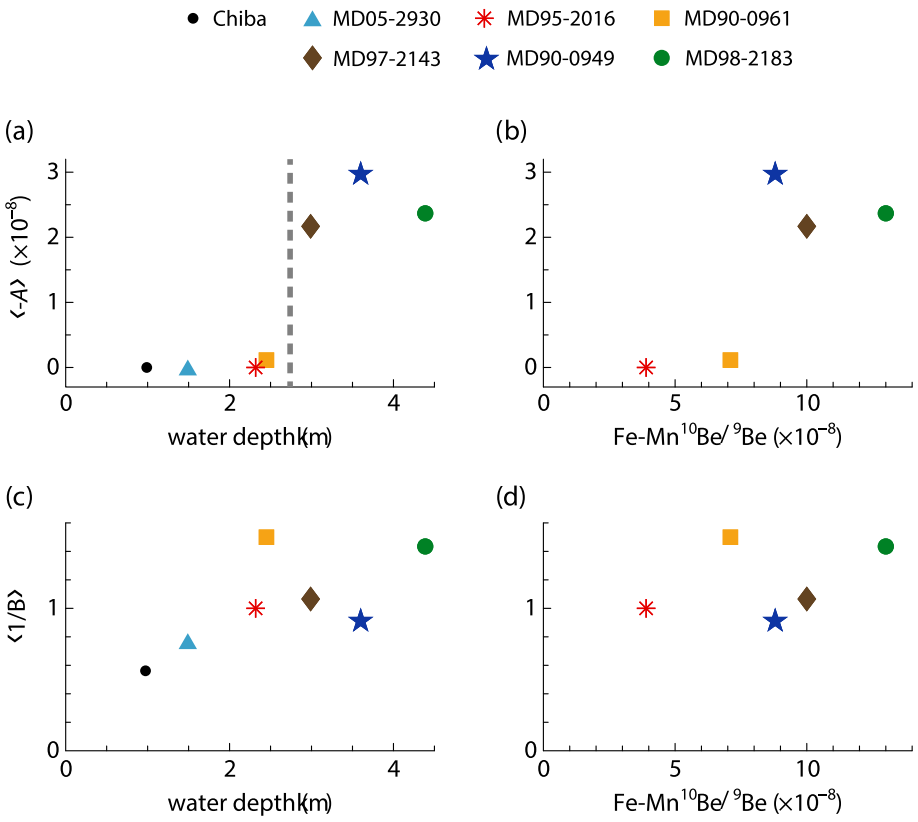


**Fig. 9.** Additive (top row) and multiplicative (bottom row) rescaling coefficients as a function of water depth (left) and of the $^{10}Be/^{9}Be$ values measured in nearby ferromanganese crusts (right, data from von Blanckenburg et al., 1996). The vertical dashed line in (a) indicate the water depth below which $^{10}Be/^{9}Be$ records contain a significant offset.

2017) and Indian (You, 2000) oceans. Large bottom water currents flowing over regions with small sedimentation rates, such as the Central Pacific, would collect and homogenize fluxes of Be released from sediment layers with a wide range of ages. Evidence in support of this mechanism is provided by the almost identical dependences of the *A* coefficients and of $^{10}Be/^{9}Be$ in ferromanganese crusts of nearby sites (Fig. 9b).

We finally observe that the synchronous components of our $^{10}Be/^{9}Be$ records show dependence on water depth (Fig. 9c) if Indian Ocean sites MD90-0961/0949 are omitted due to their close location to the coast line and consequent effects described in section 6.2. The synchronous component is also unrelated to the isotope ratios of nearby ferromanganese crusts (Fig. 9d). This further support the different origin of $^{10}Be$ inputs that contribute to the two components.

### 6.2. Site dependency of $^{10}Be/^{9}Be$ records

In the following, we compare the constant offsets and the synchronous components of the sedimentary $^{10}Be/^{9}Be$ records at the five sites analyzed in section 4, and two additional sites (Table 1) for which the data quality allowed a similar analysis with constant linear scaling coefficients (Table 2). The two additional sites are MD05-2930 from the Western Pacific (Ménabréaz et al., 2014) and the Chiba composite section (Simon et al., 2019). The mean offsets $\langle -A \rangle$ are already expressed in form of an isotopic ratio and can be directly compared with the bulk mean value $\langle R_i \rangle$. The mean coefficients $\langle 1/B \rangle$, on the other hand, express the amplitude of the synchronous component relatively to core MD95-2016, which has been chosen as reference in Section 4. These coefficients can be converted into isotope ratios by multiplying them with the average $^{10}Be/^{9}Be$ value of MD95-2016 for the 700–740 and 800–850 ka age intervals before and after the M-B reversal. The resulting mean ratios $\langle R_i^{sync} \rangle$ of the synchronous component are representative for periods of regular dipole field intensities and can be compared with modern $^{10}Be/^{9}Be$ values. The offsets, on the other hand, are representative for recycled Be contributions at any time.

Modern analogues of the synchronous $^{10}Be/^{9}Be$ component are calculated assuming the following conditions: (1) $^{10}Be$ is not recycled, that is, the only source is given by the meteoric input, (2) terrigenous $^{10}Be$ inputs are negligible, and (3) $^{10}Be$ scavenging in seawater is not affected by lateral transport. In this case, modern analogues of the synchronous components for periods of regular dipole field intensity are given by the ratio between the present-day depositional flux of meteoric cosmogenic $^{10}Be$ (Deng et al., 2020), and the mean sedimentary $^{9}Be$ flux obtained from measured $^{9}Be$ concentrations in sediment. Conditions (1) and (3) are not applicable to most sites, while condition (2) applies to open basins, far from the continental shelf, which is the case for all sites except the Chiba composite section (Simon et al., 2019).

As seen in Fig. 10, bulk isotope ratios (closed symbols) and their synchronous components (open symbols) are unrelated to modern analogues calculated with the above assumptions. A close relationship exists between bulk values and the isotope ratios of ferromanganese crusts collected at nearby sites (horizontal bars in Fig. 10), which are representative for the modern composition of deep waters (von Blanckenburg et al., 1996). Ferromanganese crust values, however, are ~2 times larger than the sedimentary counterpart at all sites. The synchronous components of all sites except those more strongly affected by terrigenous inputs (Chiba and MD05-2930), on the other hand, appear to be randomly scattered around a global average of $\sim 2.5 \times 10^{-8}$, with maximum deviations

of ±30%, as expected from good lateral mixing in open basins.

Be records of the M-B reversal obtained from continental shallow shelf/slope settings with very large sedimentation rates provide a useful term of comparison for the additive and multiplicative environmental effects discussed above. For instance, two Mediterranean sections, the Montalbano Jonico ($v_{sed} \approx$ 80 cm/ ka) (Simon et al., 2017) and the Valle di Manche ($v_{sed} \approx$25 cm/ ka) (Capraro et al., 2005), are characterized by much lower $^{10}Be/^{9}Be$ values. The mean $^{10}Be/^{9}Be$ ratio for Montalbano Jonico section estimated outside the transition (754–766 ka and 790–800 ka) is $\sim 0.32 \times 10^{-8}$, and a $\sim 0.58 \times 10^{-8}$ peak at 774 ka during the transition, whereas the mean $^{10}Be/^{9}Be$ estimated during 780–794 ka for Valle di Manche sequence is $\sim 0.14 \times 10^{-8}$ with maximum value at 774 ka $\sim 0.42 \times 10^{-8}$ (Capraro et al., 2019). Both the average and the peak values are 7–8 times smaller than those of MD95-2016, which means that the two records are roughly proportional to each other, as expected in case of negligible offsets. The large proportionality factor can be explained by the combined effect of $\sim$ 1.4 times larger and $\sim$5 times smaller authigenic $^{9}Be$ and $^{10}Be$ concentrations, respectively.

Another sequence with a similarly high sedimentation rate ($v_{sed} \approx$90 cm/ka) and shelf/slope setting (Chiba composite section, Simon et al., 2019) presents intermediate properties: average and peak $^{10}Be/^{9}Be$ values 1.8–1.9 times smaller than MD95-2016. The proportionality factor results from $\sim$1.2 and $\sim$2.1 times smaller authigenic $^{9}Be$ and $^{10}Be$ concentrations, respectively. The different $^{10}Be$ concentrations and $^{10}Be/^{9}Be$ ratios of the Montalbano and Chiba sections can be explained by the latter being situated along the large Kuroshio current in the East China Sea, fed by the North Equatorial Current (Gallagher et al., 2015). Contrary to the case of the semi-enclosed Mediterranean basin, this large current system intercepts atmospheric $^{10}Be$ far from continental $^{9}Be$ sources. Foraminiferal proxies suggest an eastward deflection of the Kuroshio current during the last glacial maximum (Haneda et al., 2020). A glacial current shift might explain the lower MIS20 $^{10}Be/^{9}Be$ values of the Chiba composite section with respect to a $^{10}Be/^{9}Be$ stack (Simon et al., 2019). Finally, the absence of significant offsets in the Montalbano and Chiba sections confirm the pelagic origin of recycled Be sources.

The temporal variability of environmental effects, revealed by synchronous term *B* and recycled component *A*, is inversely proportional to the distance from the coast (Fig. 11). Core MD90-0961, located only $\sim$38 km offshore the closest island of the Maldives atoll, is the most affected. The following mechanisms can explain the effect of coast proximity on multiplicative climatic modulations: (1) boundary scavenging, which depends on sediment flux (Anderson, 1990), (2) atmospheric scavenging, which is controlled by rainfall, with glacial-interglacial differences showing prominent coastal effects (Cao et al., 2019), and (3) boundary effects on the surface-bottom transportation matrix representing the path of settling particles (Nooteboom et al., 2019). The relation between coast proximity and recycled Be fluxes is more difficult to explain. This relation depends essentially on a single large value corresponding to MD90-0961. Given the proximity of MD90-0961 to the Maldives and the capacity of corals to incorporate dissolved Be in their lattice structure (Lal et al., 2005), coral dissolution during sea level changes represents a possible source of episodic and local recycled Be inputs. The dissolution of coral carbonates is promoted by ocean acidification (Hoegh-Guldberg et al., 2007; Andersson et Gledhill, 2013; Cyronak et al., 2016), which is expected mostly during interglacials (Anderson and Archer, 2002). Indeed, the additive coefficient of MD90-0961 becomes more negative during the MIS 19 and 21 interglacials (Fig. 8), pointing to higher recycled $^{10}Be$ fluxes. However, comparing the $^{10}Be/^{9}Be$ records from similar environmental settings over successive climatic stages would be beneficial to confirm the proposed mechanism.

## 7. Conclusions

Detailed sedimentary records of authigenic $^{10}Be$ and $^{9}Be$ during the last geomagnetic reversal at five sites from the North Atlantic, Indian, and Pacific Oceans enabled us to test the consistency of the $^{10}Be/^{9}Be$ ratio as a proxy for the global cosmogenic $^{10}Be$ production rate. Relative differences between records can be explained by a linear relationship between global $^{10}Be$ production rate and authigenic $^{10}Be/^{9}Be$, instead of the direct proportionality predicted by simple models of $^{10}Be$ transport and scavenging that are used for current reconstructions of the geomagnetic dipole moment. The additive and multiplicative coefficients associated with this linear response are site-specific and time-dependent. A detailed investigation of the dependence of $^{9}Be$ and $^{10}Be$ concentrations on the calcium carbonate content of sediment, which is one of the major factors affecting the scavenging efficiency, permits to exclude $^{10}Be/^{9}Be$ artifacts related to sediment composition.

A simple coupled model for $^{10}Be$ mass balance and scavenging has been used to confirm that the $^{10}Be/^{9}Be$ response can be represented by a linear function with climate-dependent additive and multiplicative terms. Non-zero additive terms reflect $^{10}Be$ inputs from sources with residence times $>$ 100 ka. Multiplicative terms reflect the efficiency of atmospheric and oceanic Be scavenging, which are in turn controlled by precipitation, sediment fluxes, and oceanic circulation. Reconstructing these coefficients at each site without an independent knowledge of the global $^{10}Be$ production rate is not possible.

However, it is possible to obtain solutions for relative record differences, provided that all records share a common period of time with large geomagnetic variations (in our case the M-B reversal), which is long enough to capture a full glacial-interglacial cycle. For this purpose, additive and multiplicative terms are assumed to be functions of a common global climatic signal, which we identified with benthic $\delta^{18}O$. If environmental modulation effects are sufficiently small, the climatic dependence can be linearised, obtaining a solvable set of equations. The resulting solutions lead to the following conclusions:

1. Additive inputs are relatively large, accounting for up to $\sim$60% of the average $^{10}Be/^{9}Be$ level outside the M-B reversal, with little variations over time, except for one site located near the Maldives. They thus represent a site-specific, constant offset that can be subtracted if the solution set includes at least one core that is negligibly affected. Corrected records are proportional to the global $^{10}Be$ production rate, as required by reconstructions of the geomagnetic dipole strength. The origin of the offset is related to sources of ancient $^{10}Be$ with age distributions exceeding 100 ka, which are sufficiently large to cancel geomagnetic variations. These sources might include terrigenous inputs and diagenetic fluxes from sediment at the ocean floor, whereby terrigenous inputs are not expected to play a major role at sites where $^{10}Be/^{9}Be$ is significantly enhanced by ocean water masses circulations. The recycled Be flux is unaffected by climate, and the large range of involved sediment ages yields a constant isotopic ratio. We did not find evidences for post-glacial ice melting at the North Atlantic site, but variable additive contributions have been detected at the Maldives site, presumably fed by coral reef dissolution.
2. Offsets display a step-like dependence on water depth, with a relatively sharp threshold of 2.8 km. This means that recycled Be inputs are confined to deep, old waters that are poorly mixed with overlying masses.

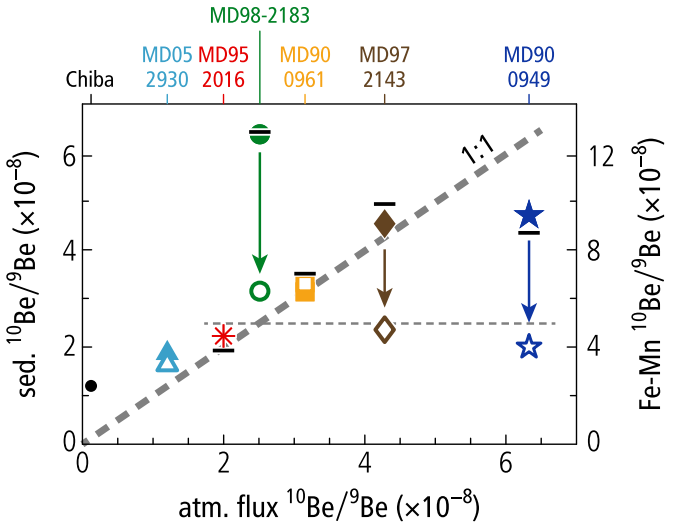


**Fig. 10.** Mean sedimentary $^{10}$Be/$^{9}$Be values (left scale, filled symbols) vs. the ratio between the modern flux of meteoric $^{10}$Be from the atmosphere (data from Deng et al., 2020) for the five sites analyzed in Section 4, and two additional sites for which a simplified analysis has been performed using constant rescaling coefficients: Chiba composite section (data from Simon et al., 2019) and MD05-2930 (data from Ménabréaz et al., 2014). Arrows points to the synchronous component of the bulk $^{10}$Be/$^{9}$Be during periods of regular dipole strength (open symbols). The thick dashed line is the 1:1 relationship between sedimentary and meteoric $^{10}$Be/$^{9}$Be values expected for an isolated water column without lateral transport. The thin horizontal dashed line is the average of the syncrhonous component for the five sites analyzed in Section 4. Bulk $^{10}$Be/$^{9}$Be values of ferromanganese crusts for nearby sites (horizontal bars) are shown for comparison (right scale, notice the factor two difference with the left scale.

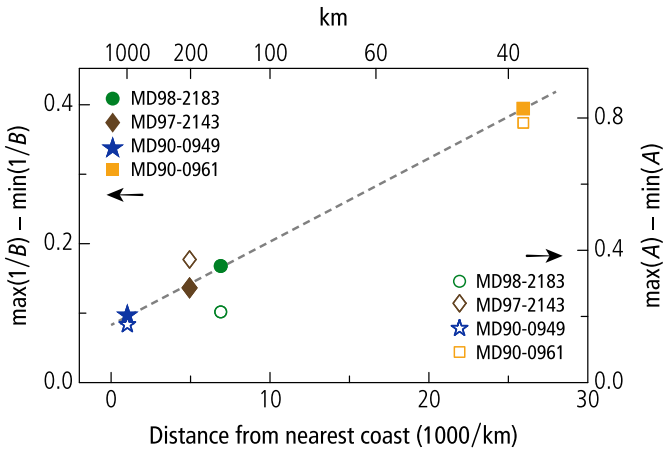


**Fig. 11.** Maximum temporal changes of additive ($A_{ij}$) and multiplicative ($B_{ij}$) climatic modulation coefficients with respect to core MD95-2016 (Table 2), vs. inverse distance from the nearest coast. The dashed line is a linear fit for the multiplicative coefficients.

3. Multiplicative environmental effects are site-specific and reflect mainly glacial-interglacial cycles. The Indian and Pacific Ocean sites display a common modulation with respect to the North Atlantic: the difference between these two groups of records oscillates with a maximum amplitude of ±10–15% relative to the maximum $^{10}$Be/$^{9}$Be increase during the M-B reversal. This amplitude is sufficiently large to mask minor dipole moment variations during stable polarity periods. Because of the lack of an absolute reference for the $^{10}$Be production rate, it is not possible to obtain absolute estimates of the multiplicative modulation at each site. Glacial-interglacial changes of atmospheric precipitation patterns, sediment delivery, and oceanic scavenging efficiency are expected to occur in the North Atlantic and in the other basins, so that it is not possible to choose a reference record with minimal environmental effects. Time averages of the multiplicative coefficients represent the total site-specific $^{10}$Be scavenging efficiency. Maximum differences between records amount to ~40%. These differences do not depend systematically on water depth, sedimentation rate, or $^{9}$Be fluxes. Differences between the sedimentary $^{10}$Be/$^{9}$Be ratios at Pacific sites are similar to the intra-basin variability of $^{10}$Be/$^{9}$Be in deep waters (von Blanckenburg et al., 2005). In the context of boundary scavenging (Anderson et al., 1990; von Blanckenburg and Igel, 1999), they can be explained by incomplete intra-basin mixing: in this case, sites with largest $^{10}$Be/$^{9}$Be values are thus those that benefit from strongest lateral mixing, which brings $^{10}$Be-rich water from the center of the basin toward the margins (Igel and von Banckenburg, 1999).
4. The environmental modulation amplitude is inversely related to the distance from the coast, with largest effects observed for a core located ~38 km offshore the closest island of the Maldives atoll. Coastal amplification of climatic effects can be explained by boundary scavenging, and by the enhanced sensitivity of atmospheric scavenging and the surface-bottom transportation matrix on coastal proximity.

While the observed environmental contamination of $^{10}$Be/$^{9}$Be records does not prevent stratigraphic recognition of large $^{10}$Be increase episodes, geomagnetic dipole moment reconstructions can benefit in several ways from the climatic modulation information gained with our modelling approach. First, a sufficiently diverse set of core locations likely contains at least one $^{10}$Be/$^{9}$Be record with most suited properties that can serve as a reference. These optimal properties are: (1) negligible Be-recycling contributions, which restores the required proportionality with the global atmospheric $^{10}$Be production rate, and (2) minimum climatic modulation amplitude, as far as it can be determined from relative comparisons between records. Based on our detailed analysis of five sedimentary cores retrieved from different geographical settings, these conditions are most likely encountered in open basins at sites (1) with <2.8 km water depth, (2) >200 km offshore, and (3) located underneath a large current system extending over regions with minimum terrigenous inputs. Scaling all records to match the chosen reference enables us to produce a $^{10}$Be/$^{9}$Be with reduced noise and artefact contributions. An example or artifacts isolated with our model is represented by incoherent short-term variations with typical periods of 20 ka, which are likely related to rectified precessional forcing of the oceanic circulation.

## Authorship contributions

Tatiana Savranskaia: Investigation, Writing – original draft, Writing – review & editing; Visualisation; Methodology; Formal analysis. Ramon Egli: Investigation, Writing – original draft, Writing – review & editing; Methodology; Formal analysis . Jean-Pierre Valet: Conceptualization; Writing – original draft; Writing – review & editing; Funding acquisition; Project administration; Supervision. Franck Bassinot: Investigation, Writing – review & editing; Resources. Laure Meynadier: Conceptualization; Writing – review & editing. Didier L. Bourlès: Writing – review & editing; Resources. Quentin Simon: Writing – review & editing; Resources. Nicolas Thouveny: Writing – review & editing; Resources

## Declaration of competing interest

The authors declare that they have no known competing

financial interests or personal relationships that could have appeared to influence the work reported in this paper.

## Acknowledgments

This study is supported by the ERC advanced grant to Jean-Pierre Valet. Grant agreement ID: 339899 - "EDIFICE", funded under the ERC's 7th Framework Program FP7-IDEAS-ERC (European Union).- The ASTER AMS national facility (CEREGE, Aix en Provence, France) is supported by INSU/CNRS, IRD and by the ANR through the EQUIPEX "ASTER-CEREGE" action. This is IPGP contribution number 4201.

## Appendix A. Supplementary data

Supplementary data to this article can be found online at https://doi.org/10.1016/j.quascirev.2021.106809.

## References

Anderson, R.F., Fleisher, M.Q., Biscaye, P.E., Kumar, N., Dittrich, B., Kubik, P., Suter, M., 1994. Anomalous boundary scavenging in the Middle Atlantic Bight: evidence from 230Th, 231Pa, 10Be and 210Pb. Deep Sea Res. Part II Top. Stud. Oceanogr. 41 (2-3), 537–561.
Anderson, D.M., 2001. Attenuation of millennial-scale events by bioturbation in marine sediments. Paleoceanography 16 (4), 352–357.
Anderson, D.M., Archer, D., 2002. Glacial–interglacial stability of ocean ph inferred from foraminifer dissolution rates. Nature 416 (6876), 70–73.
Anderson, R., Lao, Y., Broecker, W., Trumbore, S.E., Hofmann, H., Wolfli, W., 1990. Boundary scavenging in the pacific ocean: a comparison of10be and231pa. Earth Planet Sci. Lett. 96 (3–4), 287–304.
Andersson, A.J., Gledhill, D., 2013. Ocean acidification and coral reefs: effects on breakdown, dissolution, and net ecosystem calcification. Annual review of marine science 5, 321–348.
Antico, A., Marchal, O., Mysak, L.A., 2010. Time-dependent response of a zonally averaged ocean–atmosphere–sea ice model to milankovitch forcing. Clim. Dynam. 34 (6), 763–779.
Arnold, J.R., 1956. Beryllium-10 produced by cosmic rays. Science 124 (3222), 584–585.
Backman, J., Duncan, R., 1988. Shipboard scientific party. In: Proc. ODP, Init. Repts. Ocean Drilling Program, College Station, TX, p. 115.
Bacon, M., 1988. Tracers of chemical scavenging in the ocean: boundary effects and large-scale chemical fractionation. Phil. Trans. Roy. Soc. Lond. Math. Phys. Sci. 325 (1583), 147–160.
Bacon, M.P., Huh, C.-A., Fleer, A.P., Deuser, W.G., 1985. Seasonality in the flux of natural radionuclides and plutonium in the deep sargasso sea. Deep Sea Research Part A. Oceanographic Research Papers 32 (3), 273–286.
Bard, E., Rickaby, R.E., 2009. Migration of the subtropical front as a modulator of glacial climate. Nature 460 (7253), 380–383.
Bassinot, F.C., 1993. Sonostratigraphy of tropical indian ocean giant piston cores: toward a rapid and high-resolution tool for tracking dissolution cycles in pleistocene carbonate sediments. Earth Planet Sci. Lett. 120 (3–4), 327–344.
Beaufort, L., Chen, M., Droxler, A., Yokoyama, Y., Balut, Y., Rothe, S., 2005. Md148-pecten images xiii cruise report. Inst. Pol. Fr., Plouzanē, France.
Blinov, A., 1988. The dependence of cosmogenic isotope production rate on solar activity and geomagnetic field variations. In: Secular Solar and Geomagnetic Variations in the Last 10,000 Years. Springer, pp. 329–340.
Boudreau, B.P., 1998. Mean mixed depth of sediments: the wherefore and the why. Limnol. Oceanogr. 43 (3), 524–526.
Bourles, D., Raisbeck, G., Yiou, F., 1989a. 10be and 9be in marine sediments and their potential for dating. Geochem. Cosmochim. Acta 53 (2), 443–452.
Bourles, D., Klinkhammer, G., Campbell, A., Brown, E., Edmond, J., et al., 1989b. Beryllium in marine pore waters: geochemical and geochronological implications. Nature 341 (6244), 731–733.
Brickman, D., Wright, D., Hyde, W., 1999. Filtering of milankovitch cycles by the thermohaline circulation. J. Clim. 12 (6), 1644–1658.
Burdige, D.J., 1993. The biogeochemistry of manganese and iron reduction in marine sediments. Earth Sci. Rev. 35 (3), 249–284.
Cao, J., Wang, B., Liu, J., 2019. Attribution of the last glacial maximum climate formation. Clim. Dynam. 53 (3–4), 1661–1679.
Capraro, L., Asioli, A., Backman, J., Bertoldi, R., Channell, J., Massari, F., Rio, D., 2005. Climatic patterns revealed by pollen and oxygen isotope records across the matuyama-brunhes boundary in the central mediterranean (southern Italy). Geological Society, London, Special Publications 247 (1), 159–182.
Capraro, L., Tateo, F., Ferretti, P., Fornaciari, E., Macrì, P., Scarponi, D., Preto, N., Xian, F., Kong, X., Xie, X., 2019. A mediterranean perspective on 10be, sedimentation and climate around the matuyama/brunhes boundary: les liaisons dangereuses? Quat. Sci. Rev. 226, 106039.
Carcaillet, J.T., Bourlès, D.L., Thouveny, N., 2004. Geomagnetic dipole moment and 10be production rate intercalibration from authigenic 10be/9be for the last 1.3 ma. G-cubed 5 (5).
Chase, Z., Anderson, R.F., Fleisher, M.Q., Kubik, P.W., 2002. The influence of particle composition and particle flux on scavenging of th, pa and be in the ocean. Earth Planet Sci. Lett. 204 (1–2), 215–229.
Chmeleff, J., von Blanckenburg, F., Kossert, K., Jakob, D., 2010. Determination of the 10be half-life by multicollector icp-ms and liquid scintillation counting. Nucl. Instrum. Methods Phys. Res. Sect. B Beam Interact. Mater. Atoms 268 (2), 192–199.
Christl, M., 2007. Sensitivity and response of beryllium-10 in marine sediments to rapid production changes (geomagnetic events): a box model study. G-cubed 8 (9).
Christl, M., Strobl, C., Mangini, A., 2003. Beryllium-10 in deep-sea sediments: a tracer for the earth's magnetic field intensity during the last 200,000 years. Quat. Sci. Rev. 22 (5–7), 725–739.
Cyronak, T., Eyre, B.D., 2016. The synergistic effects of ocean acidification and organic metabolism on calcium carbonate (caco3) dissolution in coral reef sediments. Mar. Chem. 183, 1–12.
Das, S., Hendry, M.J., Essilfie-Dughan, J., 2011. Transformation of two-line ferrihydrite to goethite and hematite as a function of ph and temperature. Environ. Sci. Technol. 45 (1), 268–275.
Deng, K., Wittmann, H., von Blanckenburg, F., 2020. The depositional flux of meteoric cosmogenic 10be from modeling and observation. Earth Planet Sci. Lett. 550, 116530.
Dhal, S.P., Balakrishnan, S., Kumar, P., Singh, P., Sharan, A., Chopra, S., 2018. 10 be/9 be ratios of cauvery river delta sediments, southern India: implications for palaeo-denudation rates in the catchment and variation in summer monsoon rainfall during late quaternary. Curr. Sci. 115 (9), 1770.
Dong, W., Lal, D., Ransom, B., Berger, W., Caffee, M.W., 2001. Marine biogeochemistries of be and al: a study based on cosmogenic 10 be, be and al in marine calcite, aragonite, and opal. Journal of Earth System Science 110 (2), 95–102.
Elrod, V.A., Berelson, W.M., Coale, K.H., Johnson, K.S., 2004. The flux of iron from continental shelf sediments: a missing source for global budgets. Geophys. Res. Lett. 31 (12).
Elsasser, W., Ney, E., Winckler, J., 1956. Cosmic-ray intensity and geomagnetism. Nature 178 (4544), 1226.
Fantle, M.S., DePaolo, D.J., 2007. Ca isotopes in carbonate sediment and pore fluid from odp site 807a: the ca2+ (aq)–calcite equilibrium fractionation factor and calcite recrystallization rates in pleistocene sediments. Geochem. Cosmochim. Acta 71 (10), 2524–2546.
Fantle, M.S., Maher, K.M., DePaolo, D., 2010. Isotopic approaches for quantifying the rates of marine burial diagenesis. Rev. Geophys. 48 (3).
Feely, R.A., Sabine, C.L., Lee, K., Berelson, W., Kleypas, J., Fabry, V.J., Millero, F.J., 2004. Impact of anthropogenic co2 on the caco3 system in the oceans. Science 305 (5682), 362–366.
Ferrari, R., Jansen, M.F., Adkins, J.F., Burke, A., Stewart, A.L., Thompson, A.F., 2014. Antarctic sea ice control on ocean circulation in present and glacial climates. Proc. Natl. Acad. Sci. Unit. States Am. 111 (24), 8753–8758.
Field, C.V., Schmidt, G.A., Koch, D., Salyk, C., 2006. Modeling production and climate-related impacts on 10be concentration in ice cores. J. Geophys. Res.: Atmosphere 111 (D15).
Florindo, F., Roberts, A.P., Palmer, M.R., 2003. Magnetite dissolution in siliceous sediments. G-cubed 4 (7).
Frank, M., Schwarz, B., Baumann, S., Kubik, P.W., Suter, M., Mangini, A.A., 1997. 200 kyr record of cosmogenic radionuclide production rate and geomagnetic field intensity from 10be in globally stacked deep-sea sediments1. Earth Planet Sci. Lett. 149 (1), 121–129.
Gallagher, S.J., Kitamura, A., Iryu, Y., Itaki, T., Koizumi, I., Hoiles, P.W., 2015. The pliocene to recent history of the kuroshio and tsushima currents: a multi-proxy approach. Progress in Earth and Planetary Science 2 (1), 17.
Gehlen, M., Gangstø, R., Schneider, B., Bopp, L., Aumont, O., Éthé, C., 2007. The fate of pelagic caco 3 production in a high co 2 ocean: a model study. Biogeosciences 4 (4), 505–519.
Gehrke, B., Lackschewitz, K., Wallrabe-Adams, H.-J., 1996. Late quaternary sedimentation on the mid-atlantic reykjanes ridge: clay mineral assemblages and depositional environment. Geol. Rundsch. 85 (3), 525–535.
Goel, P., Jha, S., Lal, D., Radhakrishna, P., et al., 1956. Cosmic ray produced beryllium isotopes in rain water. Nucl. Phys. 1 (3), 196–201.
Guinasso Jr., N., Schink, D., 1975. Quantitative estimates of biological mixing rates in abyssal sediments. J. Geophys. Res. 80 (21), 3032–3043.
Haneda, Y., Okada, M., Kubota, Y., Suganuma, Y., 2020. Millennial-scale hydrographic changes in the northwestern pacific during marine isotope stage 19: teleconnections with ice melt in the north atlantic. Earth Planet Sci. Lett. 531, 115936.
Heikkilä, U., Smith, A., 2013. Production rate and climate influences on the variability of 10be deposition simulated by echam5-ham: globally, in Greenland, and in Antarctica. J. Geophys. Res.: Atmosphere 118 (6), 2506–2520.
Heikkilä, U., Beer, J., Feichter, J., 2008. Modeling cosmogenic radionuclides 10 be and 7 be during the maunder minimum using the echam5-ham general circulation model. Atmos. Chem. Phys. 8 (10), 2797–2809.
Heikkilä, U., Beer, J., Feichter, J., 2009. Meridional transport and deposition of atmospheric 10 be. Atmos. Chem. Phys. 9 (2), 515–527.
Heikkilä, U., Beer, J., Abreu, J., Steinhilber, F., 2013. On the atmospheric transport and deposition of the cosmogenic radionuclides (10 be): a review. Space Sci. Rev. 176

(1–4), 321–332.
Henken-Mellies, W., Beer, J., Heller, F., Hsü, K., Shen, C., Bonani, G., Hofmann, H., Suter, M., Wölfli, W., 1990. 10be and9be in south atlantic dsdp site 519: relation to geomagnetic reversals and to sediment composition. Earth Planet Sci. Lett. 98 (3–4), 267–276.
Hoegh-Guldberg, O., Mumby, P.J., Hooten, A.J., Steneck, R.S., Greenfield, P., Gomez, E., Harvell, C.D., Sale, P.F., Edwards, A.J., Caldeira, K., et al., 2007. Coral reefs under rapid climate change and ocean acidification. Science 318 (5857), 1737–1742.
Horng, C.-S., Lee, M.-Y., Palike, H., Wei, K.-Y., Liang, W.-T., Iizuka, Y., Torii, M., 2002. Astronomically calibrated ages for geomagnetic reversals within the matuyama chron. Earth Planets Space 54 (6), 679–690.
Igel, H., von Blanckenburg, F., 1999. Lateral mixing and advection of reactive isotope tracers in ocean basins: numerical modeling. GGG 1 (1), 1002–1019.
Beer, J., McCracken, R., 2012. In Cosmogenic Radionuclides. In: Ch. 10 .Production of Cosmogenic Radionuclides in the Atmosphere. Springer, pp. 139–177.
Kawabe, M., Fujio, S., Yanagimoto, D., 2003. Deep-water circulation at low latitudes in the western north pacific. Deep Sea Res. Oceanogr. Res. Pap. 50 (5), 631–656.
Kawahata, H., Yamamuro, M., Ohta, H., 1998. Seasonal and vertical variations of sinking particle fluxes in the west caroline basin. Oceanol. Acta 21 (4), 521–532.
Knudsen, M.F., Henderson, G.M., Frank, M., Mac Niocaill, C., Kubik, P.W., 2008. In-phase anomalies in beryllium-10 production and palaeomagnetic field behaviour during the Iceland basin geomagnetic excursion. Earth Planet Sci. Lett. 265 (3–4), 588–599.
Kocharov, G., Blinov, A., Konstantinov, A., Levchenko, V., 1989. Temporal 10 be and 14 c variations: a tool for paleomagnetic research. Radiocarbon 31 (2), 163–168.
Koeve, W., Wagner, H., Kähler, P., Oschlies, A., 2015. 14c-age tracers in global ocean circulation models. Geosci. Model Dev. (GMD) 8, 2079–2094.
Korschinek, G., Bergmaier, A., Faestermann, T., Gerstmann, U., Knie, K., Rugel, G., Wallner, A., Dillmann, I., Dollinger, G., Von Gostomski, C.L., et al., 2010. A new value for the half-life of 10be by heavy-ion elastic recoil detection and liquid scintillation counting. Nucl. Instrum. Methods Phys. Res. Sect. B Beam Interact. Mater. Atoms 268 (2), 187–191.
Ku, T., Kusakabe, M., Measures, C., Southon, J., Cusimano, G., Vogel, J., Nelson, D., Nakaya, S., 1990. Beryllium isotope distribution in the western north atlantic: a comparison to the pacific. Deep Sea Research Part A. Oceanographic Research Papers 37 (5), 795–808.
Kusakabe, M., Ku, T.-L., Southon, J.R., et al., 1990. Beryllium isotopes in the ocean. Geochem. J. 24 (4), 263–272.
Lal, D., Peters, B., 1967. Cosmic ray produced radioactivity on the earth. In: FLUGGE, S. (Ed.), Encyclopedia of Physics, vol. XLVI/2. Springer-Verlag, pp. 551–612. Cosmic rays II.
Lal, D., Gallup, C.D., Somayajulu, B.L., Vacher, L., Caffee, M.W., Jull, A.J., Finkel, R.C., Speed, R.C., Winter, A., 2005. Records of cosmogenic radionuclides 10be, 26al and 36cl in corals: first studies on coral erosion rates and potential of dating very old corals. Geochem. Cosmochim. Acta 69 (24), 5717–5728.
Li, Y.-H., 2005. Controversy over the relationship between major components of sediment-trap materials and the bulk distribution coefficients of 230th, 231pa, and 10be. Earth Planet Sci. Lett. 233 (1–2), 1–7.
Lisiecki, L.E., Raymo, M.E., 2005. A pliocene-pleistocene stack of 57 globally distributed benthic δ18o records. Paleoceanography 20, 1.
Luo, S., Ku, T.-L., 2004. On the importance of opal, carbonate, and lithogenic clays in scavenging and fractionating 230th, 231pa and 10be in the ocean. Earth Planet Sci. Lett. 220 (1–2), 201–211.
Maher, K., Von Blanckenburg, F., 2016. Surface ages and weathering rates from 10be (meteoric) and 10be/9be: insights from differential mass balance and reactive transport modeling. Chem. Geol. 446, 70–86.
Mangini, A., Segl, M., Bonani, G., Hofmann, H., Morenzoni, E., Nessi, M., Suter, M., Wölfli, W., Turekian, K., 1984. Mass-spectrometric 10be dating of deep-sea sediments applying the zürich tandem accelerator. Nucl. Instrum. Methods Phys. Res. Sect. B Beam Interact. Mater. Atoms 5 (2), 353–358.
Masarik, J., Beer, J., 1999. Simulation of particle fluxes and cosmogenic nuclide production in the earth's atmosphere. J. Geophys. Res.: Atmosphere 104 (D10), 12099–12111.
Masarik, J., Beer, J., 2009. An updated simulation of particle fluxes and cosmogenic nuclide production in the earth's atmosphere. J. Geophys. Res.: Atmosphere 114 (D11).
Mayer, L., Pisias, N., Janecek, T., 1992. Shipboard scientific party,1992: site 851. In: Proc Ocean Drill Program Initial Rep, vol. 138, pp. 891–965.
McCAVE, I., 1975. Vertical flux of particles in the ocean. In: Deep Sea Research and Oceanographic Abstracts, vol. 22. Elsevier, pp. 491–502.
McHargue, L., Damon, P., 1991. The global beryllium 10 cycle. Rev. Geophys. 29 (2), 141–158.
Measures, C., Edmond, J., 1983. The geochemical cycle of 9be: a reconnaissance. Earth Planet Sci. Lett. 66, 101–110.
Measures, C., Ku, T., Luo, S., Southon, J., Xu, X., Kusakabe, M., 1996. The distribution of 10be and 9be in the south atlantic. Deep Sea Res. Oceanogr. Res. Pap. 43 (7), 987–1009.
Ménabréaz, L., Bourlès, D., Thouveny, N., 2012. Amplitude and timing of the laschamp geomagnetic dipole low from the global atmospheric 10be overproduction: contribution of authigenic 10be/9be ratios in west equatorial pacific sediments. J. Geophys. Res.: Solid Earth 117 (B11).
Ménabréaz, L., Thouveny, N., Bourlès, D.L., Vidal, L., 2014. The geomagnetic dipole moment variation between 250 and 800 ka bp reconstructed from the authigenic 10 be/9 be signature in west equatorial pacific sediments. Earth Planet Sci. Lett. 385, 190–205.
Moritz, H., 1978. Least-squares collocation. Rev. Geophys. 16 (3), 421–430.
Nooteboom, P.D., Bijl, P.K., van Sebille, E., von der Heydt, A.S., Dijkstra, H.A., 2019. Transport bias by ocean currents in sedimentary microplankton assemblages: implications for paleoceanographic reconstructions. Paleoceanography and Paleoclimatology 34 (7), 1178–1194.
Paul, A., Schäfer-Neth, C., 2003. Modeling the water masses of the atlantic ocean at the last glacial maximum. Paleoceanography 18 (3).
Piper, D.Z., Williamson, M.E., 1977. Composition of pacific ocean ferromanganese nodules. Mar. Geol. 23 (4), 285–303.
Poluianov, S., Kovaltsov, G.A., Mishev, A.L., Usoskin, I.G., 2016. Production of cosmogenic isotopes 7be, 10be, 14c, 22na, and 36cl in the atmosphere: altitudinal profiles of yield functions. J. Geophys. Res.: Atmosphere 121 (13), 8125–8136.
Raisbeck, G., Yiou, F., Fruneau, M., Loiseaux, J., Lieuvin, M., Ravel, J., Reyss, J., Guichard, F., 1980. 10be concentration and residence time in the deep ocean. Earth Planet Sci. Lett. 51 (2), 275–278.
Raisbeck, G., Yiou, F., Bourles, D., Kent, D.V., 1985. Evidence for an increase in cosmogenic 10be during a geomagnetic reversal. Nature 315 (6017), 315.
Raisbeck, G., Yiou, F., Jouzel, J., Stocker, T., 2007. Direct north-south synchronization of abrupt climate change record in ice cores using beryllium 10. Clim. Past 3 (3), 541–547.
Richter, F.M., DePaolo, D.J., 1987. Numerical models for diagenesis and the neogene sr isotopic evolution of seawater from dsdp site 590b. Earth Planet Sci. Lett. 83 (1–4), 27–38.
Rickaby, R., Bard, E., Sonzogni, C., Rostek, F., Beaufort, L., Barker, S., Rees, G., Schrag, D., 2007. Coccolith chemistry reveals secular variations in the global ocean carbon cycle? Earth Planet Sci. Lett. 253 (1–2), 83–95.
Rippert, N., Max, L., Mackensen, A., Cacho, I., Povea, P., Tiedemann, R., 2017. Alternating influence of northern versus southern-sourced water masses on the equatorial pacific subthermocline during the past 240 ka. Paleoceanography 32 (11), 1256–1274.
Ruddiman, W., McIntyre, A., 1976. Northeast atlantic paleoclimatic changes over the past 600,000 years. In: Investigation of Late Quaternary Paleoceanography and Paleoclimatology, vol. 145. Geol. Soc. of America Mem, pp. 111–146.
Schmittner, A., Clement, A.C., 2002. Sensitivity of the thermohaline circulation to tropical and high latitude freshwater forcing during the last glacial-interglacial cycle. Paleoceanography 17 (2), 7–1.
Seidov, D., Sarnthein, M., Stattegger, K., Prien, R., Weinelt, M., 1996. North atlantic ocean circulation during the last glacial maximum and subsequent meltwater event: a numerical model. J. Geophys. Res.: Oceans 101 (C7), 16305–16332.
Sharma, P., Mahannah, R., Moore, W., Ku, T., Southon, J., 1987. Transport of10be and9be in the ocean. Earth Planet Sci. Lett. 86 (1), 69–76.
Simon, Q., Thouveny, N., Bourlès, D.L., Valet, J.-P., Bassinot, F., Ménabréaz, L., Guillou, V., Choy, S., Beaufort, L., 2016a. Authigenic 10be/9be ratio signatures of the cosmogenic nuclide production linked to geomagnetic dipole moment variation since the brunhes/matuyama boundary. J. Geophys. Res.: Solid Earth 121 (11), 7716–7741.
Simon, Q., Thouveny, N., Bourles, D.L., Nuttin, L., Hillaire-Marcel, C., St-Onge, G., 2016b. Authigenic 10 be/9 be ratios and 10 be-fluxes (230 th xs-normalized) in central baffin bay sediments during the last glacial cycle: paleoenvironmental implications. Quat. Sci. Rev. 140, 142–162.
Simon, Q., Bourlès, D.L., Bassinot, F., Nomade, S., Marino, M., Ciaranfi, N., Girone, A., Maiorano, P., Thouveny, N., Choy, S., et al., 2017. Authigenic 10be/9be ratio signature of the matuyama–brunhes boundary in the montalbano jonico marine succession. Earth Planet Sci. Lett. 460, 255–267.
Simon, Q., Bourlès, D.L., Thouveny, N., Horng, C.-S., Valet, J.-P., Bassinot, F., Choy, S., 2018a. Cosmogenic signature of geomagnetic reversals and excursions from the réunion event to the matuyama–brunhes transition (0.7–2.14 ma interval). Earth Planet Sci. Lett. 482, 510–524.
Simon, Q., Thouveny, N., Bourlès, D.L., Bassinot, F., Savranskaia, T., Valet, J.-P., Team, A., et al., 2018b. Increased production of cosmogenic 10 be recorded in oceanic sediment sequences: information on the age, duration, and amplitude of the geomagnetic dipole moment minimum over the matuyama–brunhes transition. Earth Planet Sci. Lett. 489, 191–202.
Simon, Q., Suganuma, Y., Okada, M., Haneda, Y., Team, A., et al., 2019. High-resolution 10be and paleomagnetic recording of the last polarity reversal in the chiba composite section: age and dynamics of the matuyama–brunhes transition. Earth Planet Sci. Lett. 519, 92–100.
Simon, Q., Thouveny, N., Bourlès, D.L., Valet, J.-P., Bassinot, F., 2020. Cosmogenic 10be production records reveal dynamics of geomagnetic dipole moment (gdm) over the laschamp excursion (20–60 ka). Earth Planet Sci. Lett. 550, 116547.
Solan, M., Ward, E.R., White, E.L., Hibberd, E.E., Cassidy, C., Schuster, J.M., Hale, R., Godbold, J.A., 2019. Worldwide measurements of bioturbation intensity, ventilation rate, and the mixing depth of marine sediments. Scientific data 6 (1), 1–6.
Southon, J., Ku, T., Nelson, D., Reyss, J., Duplessy, J., Vogel, 1987. J. 10be in a deep-sea core: implications regarding10be production changes over the past 420 ka. Earth Planet Sci. Lett. 85 (4), 356–364.
Staubwasser, M., von Blanckenburg, F., Schoenberg, R., 2006. Iron isotopes in the early marine diagenetic iron cycle. Geology 34 (8), 629–632.
Subhas, A.V., Rollins, N.E., Berelson, W.M., Dong, S., Erez, J., Adkins, J.F., 2015. A novel determination of calcite dissolution kinetics in seawater. Geochem. Cosmochim. Acta 170, 51–68.
Suganuma, Y., Yokoyama, Y., Yamazaki, T., Kawamura, K., Horng, C.-S., Matsuzaki, H.,

2010. 10 be evidence for delayed acquisition of remanent magnetization in marine sediments: implication for a new age for the matuyama–brunhes boundary. Earth Planet Sci. Lett. 296 (3), 443–450.
Tachikawa, K., Cartapanis, O., Vidal, L., Beaufort, L., Barlyaeva, T., Bard, E., 2011. The precession phase of hydrological variability in the western pacific warm pool during the past 400 ka. Quat. Sci. Rev. 30 (25–26), 3716–3727.
Tchernia, P., 1980. Descriptive Regional Oceanography. Pergamon Press, Oxford.
Tuenter, E., Weber, S., Hilgen, F., Lourens, L., Ganopolski, A., 2005. Simulation of climate phase lags in response to precession and obliquity forcing and the role of vegetation. Clim. Dynam. 24 (2–3), 279–295.
Valet, J.-P., 2003. Time variations in geomagnetic intensity. Rev. Geophys. 41 (1).
Valet, J.-P., Bassinot, F., Bouilloux, A., Bourlès, D., Nomade, S., Guillou, V., Lopes, F., Thouveny, N., Dewilde, F., 2014. Geomagnetic, cosmogenic and climatic changes across the last geomagnetic reversal from equatorial indian ocean sediments. Earth Planet Sci. Lett. 397, 67–79.
Valet, J.-P., Meynadier, L., Simon, Q., Thouveny, N., 2016. When and why sediments fail to record the geomagnetic field during polarity reversals. Earth Planet Sci. Lett. 453, 96–107.
Valet, J.-P., Bassinot, F., Simon, Q., Savranskaia, T., Thouveny, N., Bourlés, D.L., Villedieu, A., 2019. Constraining the age of the last geomagnetic reversal from geochemical and magnetic analyses of atlantic, indian, and pacific ocean sediments. Earth Planet Sci. Lett. 506, 323–331.
Von Blanckenburg, F., Bouchez, J., 2014. River fluxes to the sea from the oceanÊ¼s 10be/9be ratio. Earth Planet Sci. Lett. 387, 34–43.
von Blanckenburg, F., Igel, H., 1999. Lateral mixing and advection of reactive isotope tracers in ocean basins: observations and mechanisms. Earth Planet Sci. Lett. 169 (1–2), 113–128.
Von Blanckenburg, F., O'nions, R., Belshaw, N., Gibb, A., Hein, J., 1996. Global distribution of beryllium isotopes in deep ocean water as derived from feî— mn crusts. Earth Planet Sci. Lett. 141 (1–4), 213–226.
von Blanckenburg, F., Bouchez, J., Wittmann, H., 2012. Earth surface erosion and weathering from the 10be (meteoric)/9be ratio. Earth Planet Sci. Lett. 351, 295–305.
Von Blanckenburg, F., Bouchez, J., Ibarra, D.E., Maher, K., 2015. Stable runoff and weathering fluxes into the oceans over quaternary climate cycles. Nat. Geosci. 8 (7), 538–542.
Walter, D., Buxbaum, G., Laqua, W., 2001. The mechanism of the thermal transformation from goethite to hematite. J. Therm. Anal. Calorim. 63 (3), 733–748.
Wei, K.-Y., Lee, T.-Q., et al., 1998. Nannofossil biochronology of tephra layers in core md972143, benham rise, western philippine sea. Terr. Atmos. Ocean Sci. 9 (1), 153–163.
Wittmann, H., Von Blanckenburg, F., Bouchez, J., Dannhaus, N., Naumann, R., Christl, M., Gaillardet, J., 2012. The dependence of meteoric 10be concentrations on particle size in amazon river bed sediment and the extraction of reactive 10be/9be ratios. Chem. Geol. 318, 126–138.
Wittmann, H., von Blanckenburg, F., Dannhaus, N., Bouchez, J., Gaillardet, J., Guyot, J.-L., Maurice, L., Roig, H., Filizola, N., Christl, M., 2015. A test of the cosmogenic 10be (meteoric)/9be proxy for simultaneously determining basin-wide erosion rates, denudation rates, and the degree of weathering in the amazon basin. J. Geophys. Res.: Earth Surface 120 (12), 2498–2528.
Wittmann, H., von Blanckenburg, F., Mohtadi, M., Christl, M., Bernhardt, A., 2017. The competition between coastal trace metal fluxes and oceanic mixing from the 10be/9be ratio: implications for sedimentary records. Geophys. Res. Lett. 44 (16), 8443–8452.
Yamazaki, T., Oda, H., 2004. Intensity-inclination correlation for long-term secular variation of the geomagnetic field and its relevance to persistent non-dipole components. Timescales of the Paleomagnetic Field 287–298.
You, Y., 2000. Implications of the deep circulation and ventilation of the indian ocean on the renewal mechanism of north atlantic deep water. J. Geophys. Res.: Oceans 105 (C10), 23895–23926.
Yu, Z., Wan, S., Colin, C., Yan, H., Bonneau, L., Liu, Z., Song, L., Sun, H., Xu, Z., Jiang, X., et al., 2016. Co-evolution of monsoonal precipitation in east asia and the tropical pacific enso system since 2.36 ma: new insights from high-resolution clay mineral records in the west philippine sea. Earth Planet Sci. Lett. 446, 45–55.
Zhou, W., Warren Beck, J., Kong, X., An, Z., Qiang, X., Wu, Z., Xian, F., Ao, H., 2014. Timing of the brunhes-matuyama magnetic polarity reversal in Chinese loess using 10be. Geology 42 (6), 467–470.
Zou, S., Lozier, S., Zenk, W., Bower, A., Johns, W., 2017. Observed and modeled pathways of the Iceland scotland overflow water in the eastern north atlantic. Prog. Oceanogr. 159, 211–222.